RSC Advances

PAPER

View Article Online
View Journal | View Issue

Cite this: *RSC Adv.*, 2023, **13**, 16047

N-Phenyl acrylamide-incorporated porous silica-bound graphene oxide sheets with excellent removal capacity for Cr(III) and Cr(VI) from wastewater

Musa Khan,[a] Faiz Ali, *[a] Saba Ramzan[b] and Zeid A. AlOthman [c]

The sophisticatedly altered Hummer's and sol–gel procedures were applied for the synthesis of graphene oxides and porous silica monolith particles respectively. The Fischer esterification protocol was used for coupling silica monoliths with graphene oxides. A *N*-phenyl acrylamide-incorporated porous polymer was synthesized at the surface of composites *via* reversible addition fragmentation chain transfer polymerization. The composition was confirmed by Fourier transform infra-red spectroscopy, FE-SEM, X-ray diffraction, zeta potential (zeta pH), Brunauer–Emmett–Teller (BET/BJH) analysis, and EDAX analysis. The resulting polymer-bound composite efficiently removed Cr(VI) and Cr(III) from waste water. Adsorption parameters such as contact time, pH effect, temperature, and adsorbent and adsorbate concentration were optimized for the optimal output of the composite. The kinetic and equilibrium models were applied to the adsorption of Cr(VI) and Cr(III) at the adsorbent surface. The maximum adsorption capacity (q_e) of Cr(VI) and Cr(III) was found to be 298.507 mg g^{-1} and 401.874 mg g^{-1}, respectively, using the same initial concentration of Cr(VI) and Cr(III) [10–60 ppm]. The adsorption data of both states of the Cr-metal followed the pseudo 2nd-order kinetic model with regression values of 0.996 ~ Cr(VI) and 0.999 ~ Cr(III) at ambient temperature. Similarly, the adsorption data of Cr(VI) best fit into the Langmuir adsorption isotherm (R^2 = 0.972) while that of Cr(III) followed the Freundlich model (R^2 = 0.983).

Received 18th April 2023
Accepted 15th May 2023

DOI: 10.1039/d3ra02568c

rsc.li/rsc-advances

Introduction

Air and water are necessary for the sustainability of life. The presence of toxic metals in different water bodies is life-threatening and their elimination is tremendously important.[1] In view of the guidelines of the Environmental Protection Agency (EPA), the two oxidation states of chromium metal, namely, VI and III present in the aquatic environment are very toxic.[2] To date, the reported sources of chromium are industries such as textiles, mining, papers, aluminium casting, inks, electroplating, cement, inorganic chemicals, steel fabrication, paints, metal cleaning, and fertilizers.[3] Various health issues are caused by water contamination with toxic metals, for which the permissible limit is only few nanograms or picograms.[4] The minimal standard reported/set by the Ministry of Environment and Forests (Government of India) for the safe effluent discharge of Cr(VI) from industries is less than 0.1 mg L^{-1}.[5] The increase in the amount of Cr(VI) in different water bodies, which might cause diseases such as skin irritation, carcinomas, liver damage, and pulmonary blocking, is a major concern across the globe.[6] Its salts are highly water soluble at all pH values.

Cr(VI) exist as hydrogen chromate $HCrO_4^{2-}$ at pH 1 and 6 in solutions and as chromate CrO_4^{2-} at a pH higher than 7. Similarly, it exists in the form of chromate, hydrogen chromate, and dichromate ($Cr_2O_7^{2-}$) at normal pH.[7] Various techniques are available for the removal of Cr(III) and Cr(VI) from wastewater including membrane filtration,[8] electro-deposition,[9] ion-exchange,[10] biological treatment processes,[11] and adsorption.[12] However, all these techniques are not widely used due to their respective disadvantages such as involvement of expensive equipment, incomplete removal of metals, and generation of toxic impurities and their monitoring.[13] Adsorption is a reliable, inexpensive, easy, and effective technique for the removal of heavy metals from industrial effluents.[14] The comparison of various wastewater treatment techniques along with their relative advantages and disadvantages is given in Table 1.[14–25] Metal organic frameworks (MOFs) are a class of recently available adsorbent materials, but they have limited practicability in the treatment of water because of their intrinsically fragile nature and poor processing.[26] Cr(III) is stable in a reducing

[a]*Department of Chemistry, University of Malakand, Chakdara Dir(L), KPK, Pakistan. E-mail: faizy186@gmail.com*

[b]*Faculty of Basic and Applied Sciences, Department of Chemistry, University of the Poonch, Rawalakot, AJK, Pakistan*

[c]*Department of Chemistry, College of Science, King Saud University, Riyadh 11451, Saudi Arabia*

environment, where it is present in cationic form $Cr(OH)_2^+$ at pH 4 to 8. Cr(III) was removed from waste water by a chemical precipitation method, which can reduce the Cr(III) concentration down to 20 mg L^{-1} from 300 mg L^{-1} or an even higher concentration. The adsorption capability of carbon-based materials toward heavy metals is low due to the presence of limited functional groups.[27] Zinc oxide (ZnO) with high energy nanosheets of different surface sizes was used as an efficient photocatalyst for the simultaneous adsorption of Cr(III) and reduction of Cr(IV). The application of ZnO was limited due to the availability of already low-energy materials.[28]

Quite enough literature is available on the adsorption of Cr(III) and Cr(VI).[29–31] Graphene oxide (GO)-based composite derivatives are effective adsorbent materials due to the high negative charge density, large surface area, and the presence of hydroxyl, epoxy, and carboxylic functional groups.[32] Despite these properties, the direct use of GO as an adsorbent material will not be a wise approach owing to the presence of oxygen-containing functional groups. The oxygen-containing functional groups act as the hard ligand.[33] The hard ligands have very limited ability to adsorb the metals/pollutants from industrial effluents in the absence of other groups.[34] Further, when the GO is used alone as an adsorbent material, its separation from the effluents during the centrifugation process is difficult.[35] Thus, several GO-based composite adsorbent materials have been synthesized for the separation of different pollutants/metals from waste water.[36–39] The GO-derived materials can easily be synthesized owing to the modification capability of the GO. The functional groups of GO react with the functional groups ($-NH_2$, –SH, –COOH, and –OH) of other materials such as silica and the resulting materials can be used for the enhanced adsorption of the target pollutants/metals present in effluents.[40]

Silica-based composites are stable and aqua-friendly materials and can be used as efficient adsorbents for the removal of heavy metals.[41] Broad dimensions (large surface area and wide pore size) of the silica-based adsorbents are effective for the improved adsorption of heavy metals.[42] The presence of silanol groups at the silica surface makes it susceptible for the composite and polymer formation when coupled with other materials.[43,44]

Various raw materials were used to prepare more efficient multifunctional adsorbents for the effective removal of pollutants from industrial effluents. Various functional groups present at the surface of GO (COC, OH, and COOH) enable it to bind chemically with other materials. The unfunctionalized GO is unstable which makes its recovery difficult after application. The unmodified GO may cause issue in centrifugation and block pores of filter papers during filtration. The binding of

Table 1 Comparison of different wastewater treatment techniques

Water treatment technology	Examples	Advantages	Disadvantages
Precipitation/ coagulation	Mg/Al/Si/Fe pre-polymerized coagulants (Tolkou *et al.*, 2019)[14]	• Mostly used and established techniques • Highly efficient • More effective techniques for large scale water treatment	• pH of the water must be imperative • High maintenance and expensive • Formation of by products and sludge
Electrochemical	Ti_4O_7 membrane anode (Le *et al.*, 2019)[15]	• Highly efficient	• The electrode can break down over time
	SnO_2/RuO_2 nanofibers (Kim *et al.*, 2019)[16]	• Highly selective • Reduced risk of secondary pollutant	• Requires high maintenance Wastewater must be highly conductive
Biological treatment	Membrane bioreactor[17] (Luo *et al.*, 2014)[18] Aerobic granules (Zhang *et al.*, 2016)[19]	• Low operational cost • Efficient degradation • Handling of large volumes of water	• Sludge production Emission of greenhouse gases
Ion exchange	Polyaniline Zr(IV) iodate nanocomposite	• Easy operation	• Due to cost of resins it is expensive
	(Khan, 2020) Cu^{2+}-MOF	• Highly selective	• Operational only
	(Shao *et al.*, 2019 (ref. 20)	• Highly efficient	• The presence of other ions hindered the efficiency
Microwave catalysis	CuO/CeO_2 catalyst (Xu *et al.*, 2014)[21]	• With reduced time of reaction	• It requires high power input
	Carbon sphere templated $Ce/LaCo_{0.5}Cu_{0.5}O_3$ catalyst (Wang *et al.*, 2020)[22]	• With efficient degradation	• It requires a catalyst of microwave absorbing
Membrane filtration	Amyloid–carbon hybrid membrane (Bolisetty and Mezzenga, 2016)[23]	• Efficient degradation	• Have reduced flow rates
	$(CuFe_2O_4)$@CNT membrane (Luan *et al.*, 2019)[24]	• Automated operation • At low temperature operational	• Closing the pores easily • Requires enough maintenance
Adsorption	MIEX resin (Yang *et al.*, 2020b)[25]	• Low energy demands	• It required pH adjustment
	Composite and polymers (current study)	• An efficient and highly reliable techniques • Recyclable and effective • Having wide choice of adsorbents	• Sludge and by-product formation • Declines progressively by recyclization

monolithic silica into the sheets of GO increases its stability and can easily be handled.[45,46] The adsorption capability of silica composite materials toward heavy metals is quite higher due to large surface/volume ratio and large pore size.

In the current study, silica monolith-bound GO was synthesized by the modified Fischer esterification protocol using silica monoliths and GOs. The composite was subjected to reversible addition fragmentation chain transfer (RAFT) polymerization using *N*-phenyl acrylamide as the monomer. The resulting organic–inorganic hybrid material was used as an effective adsorbent for the removal of Cr(VI) and Cr(III) due to the large surface area (264.899 $m^2\ g^{-1}$), wide pore size, and presence of multiple functional groups. The adsorption capacity in terms of K_F values for Cr(III) and Cr(VI) is 138.653 mg g^{-1} and 401.874 mg g^{-1} respectively. The GO not only provides different functional groups but also reduces Cr(VI) into Cr(III). The philosophy behind the development of the composite in the current project is the preparation of an adsorbent material with multifactor characteristics contributing towards very efficient adsorption of heavy metals such as Cr(VI) and Cr(III) and the application of such a robust adsorbent material in real water samples collected from different sources. The resulting polymer-bound composite sheets came out to be very efficient adsorbent materials for the removal of Cr(III) and Cr(VI) from industrial effluents.

Materials and methods

Chemicals and materials

Analytical grade chemicals were used. K_2CrO_4 (Mol wt 194.17 g mol^{-1}) and $CrCl_3$ (Mol wt 158.49 g mol^{-1}) obtained from Sigma Aldrich were used as the precursors/sources of Cr(VI) and Cr(III) respectively. Urea, glacial acetic acid, and polyethylene glycol (PEG) standard were purchased from Sigma Aldrich, which were used for the synthesis of silica monoliths without further purification. *N*-Phenyl acrylamide, NaOH, HCl (37%), $NaNO_3$, H_2O_2, and $KMnO_4$ were purchased from Sigma Aldrich. The reagents of Briton Robinson buffer, H_3BO_3 (China), H_3PO_4, and CH_3COOH (Sigma Aldrich) were used for the desired pH adjustment of different solutions.

Instrumentation

Atomic absorption spectrophotometry (model-1601 from Shimadzu Japan) was performed for the detection and measurement of Cr(VI) and Cr(III). A hot plate/magnetic stirrer (Irmico, Germany), 0–2000 rpm, 285–600 °C, was used for stirring and heating. A muffle furnace (Germany, Nabertherm) at 550 °C was used for the calcination of monolithic silica to remove the impurities before reacting with GO. A centrifuge (Witeg, Germany) was used for the centrifugation of adsorbents. A pH meter (Hanna, USA) was used for pH measurement, and a sonicator (South Korean, Power sonic-405) was also employed in the current study. The shaking processes were carried out using an Orbital shaker (Taiwan).

The successful synthesis of *N*-phenyl acrylamide-incorporated porous silica-bound graphene oxide sheets was confirmed by field emission scanning electron microscopy (FE-SEM), Fourier transform infrared (FTIR) spectroscopy, Brunauer–Emmett–Teller (BET) analysis, zeta potential (zeta pH), energy-dispersive X-ray (EDX) spectroscopy and X-ray diffraction (XRD) analysis. The adsorption of Cr(VI) and Cr(III) was confirmed by BET analysis, EDX spectroscopy, and Ultra violet (UV)-visible spectrophotometry.

The BET isotherm linear plots were constructed by the techniques making use of the nitrogen adsorption–desorption on the surface of the polymer materials. The specific surface area and BET pore size distribution of the materials using the Mesh No. 16 American standard and testing materials [ASTM E:11] were carried out using a volumetric gas adsorption instrument (e series, 2000, Quanta chrome NOVA, USA) with nitrogen as the adsorption gas. The adsorption was carried out at a relative pressure of $P/P_0 = 0.96$ at 75.4 K using nitrogen gas. For the accurate measurement of pore size, pore volume, and surface area, the resulting polymer materials were vacuum heated at 100 °C for 8 h to remove the moisture adsorbed at the composite surface.[47] Excalibur spectrometer fitted with a standard detector was used for the FTIR study. KBr pellets were applied for the analysis of different functional groups located at the surface of GO, silica monoliths, silica-bound GO, and polymer-bound composites. The subsequent spectra with 5 cm^{-1} resolution in the frequency region from 4000 to 400 cm^{-1} were recorded in accordance with ref. 48. A Nano tract II Zeta analyser was used for the zeta potential measurement of the polymer-bound composite, silica monolith, and GO suspended in water. The suspension of the sample was filled in the zeta cell after cleaning the cell with paper. The zeta cell was taken in a zeta analyzer (nano trac II zeta analyzer, U zeta cell USA). The analysis of all the samples was performed at equilibration for 3 min with a manual 100 nV applied voltage at a temperature of 0.4 °C.[49,50]

Synthesis of silica particles and graphene oxide sheets

The sophisticatedly altered sol–gel protocol reported by Ali *et al.*[51] was used for the synthesis of silica particles having a monolithic architecture. First, 1650 mg PEG and 1620 mg urea were taken in a Teflon vial containing 15 mL (0.01 molar) acetic acid solution. The mixture was kept under stirring conditions for 15 min preferably below 4 °C. Then, 5 mL of the silica precursor trimethoxy silane (TMOS) was added to the mixture and stirred for 50 min. The resulting mixture was heat treated at 40 °C for 40 h in a L_c oven followed by heating in an autoclave using a GC oven at 125 °C for 30. The excess water produced during sol–gel process was decanted off. The resulting silica monolith was vacuumed dried at 60 °C for 25 h. The silica was grounded using a mortar and pestle for 12 min and finally calcined in a muffle furnace at 400 °C.

The altered Hummer's protocol was used for the synthesis of GO sheets, whereby a mixture of sodium nitrate (2.00 mg) and graphite powder (3.00 mg) were taken in 70 mL H_2SO_4 (98%). The reaction mixture was taken in a 500 mL two-necked round-bottomed flask and its temperature was kept below 20 °C.[52] The powdered $KMnO_4$ (10 mg) was added to the reaction mixture

and stirred for 3 h. The reaction mixture was kept under stirring for 3 h in an oil bath at 40 °C. Distilled water (40 mL) was added dropwise to the solution through dropping funnels. The solution colour was changed from dark to yellow. H_2O_2 was added to the reaction mixture and stirred for 3 h. The GO sheets were obtained after cooling and filtration, and washed with HCl/2-propanol/water (1 : 1 : 10 v/v%).[53]

Silica-bound graphene oxide sheets

The silica and graphene oxide were used as the raw materials in a 3 : 1 proportion in the synthesis of silica-anchored GO by the Fisher esterification protocol. The silica monolith (0.32 g) was dispersed in distilled water (50 mL) and graphene oxide (0.11 g) was dispersed in distilled water (100 mL) followed by sonication for 40 minutes. The two suspensions were mixed in a round-bottomed flask (500 mL) with the addition of 1.0 mL H_2SO_4 (98%). The whole mixture was heated at 100 °C for 24 h under reflux conditions.[54] The reaction mechanisms are illustrated in Fig. 1.

Synthesis of polymer-bound composites

An initiator-bound silica-anchored GO was synthesized by refluxing the silica-anchored GO materials taken in 25 mL toluene and a solution of 3-amino propyl trimethoxy silane (3 mL) in 5 mL toluene (anhydrous). The reaction mixture was refluxed at 110 °C for 48 h in a N_2-purging environment. The product was repeatedly washed with toluene and acetone, filtered, and dried at ambient temperature overnight.

The ligand-loaded silica@GO particles were suspended in dimethyl formamide and subjected to the reflux condensation at 54 °C for 20 h. Meanwhile, a solution containing sodium diethyldithiocarbamate (900 mg) in 10 mL dimethyl formamide was slowly added to the reaction mixture under reflux conditions. The resulting product was washed with DMF followed by the mixture containing methanol/water (60 : 40 v/v%) and finally with acetone. The product was filtered and dried overnight in a vacuum desecrator.

Finally, 5 mL *N*-phenyl acrylamide dissolved in 10 mL toluene was added slowly to the reaction mixture containing the initiator-loaded silica@GO (600 mg) dispersed in 40 mL toluene in a round-bottomed flask. RAFT polymerization was carried out at 110 °C under reflux conditions for 15 h in a nitrogen purging environment.[55–58] The resulting *N*-phenyl acrylamide-modified silica@GO was washed with acetone and dried at 65 °C overnight. The scheme of polymer synthesis is illustrated in Fig. 1.

Batch adsorption, isotherm, and kinetic studies

The adsorption efficiency of *N*-phenyl acrylamide-modified silica@GO was evaluated for the removal of Cr(III) and Cr(VI) from various effluents. The optimization studies on pH effect, temperature effect, adsorbate/adsorbent dose, and contact time were demonstrated for the maximum output of the polymer-modified composite for the removal of Cr(VI) and Cr(III).[59] Then, 8 mg of the composite, 30 mg L^{-1} for (VI), and pH 2 were found as the optimized indicators for the maximum adsorption of Cr(VI). Similarly, 6.0 mg of the composite, 40 mg L^{-1} of Cr(III), and pH 5 were found optimized for the maximum output of the adsorbent for the removal of Cr(III). All the solutions of Cr(VI) and Cr(III) were shacked using an orbital shaker for the contact time optimization while an atomic absorption spectrometer was used for the detection and measurement of the metal ions. The adsorption capacities and percentage of adsorptions for Cr(VI) and Cr(III) were computed using the following equations.

$$Q_e = \frac{(C_i - C_e)V}{W} \quad (1)$$

$$\%\ \text{Adsorption} = \frac{C_i - C_e}{C_i} \times 100 \quad (2)$$

where "C_e" and "C_i" are the equilibrium and initial metal ion concentration in mg L^{-1} respectively. "W" is the weight of adsorbent taken in mg g^{-1}, while "V" is the volume of the liquid in litres. The absorbed/unabsorbed metal amounts were detected, and their percent adsorption was computed using optimized conditions.

The isothermal studies were carried out by adding the polymer modified composite (8 g L^{-1}) ~ Cr(VI) and 2 g L^{-1} ~ Cr(III) to many flasks having different concentrations (10–50 mg L^{-1}) of the metal ions at the optimized pH (Cr(VI) ~ 2 and Cr(III) ~ 5). The mixture of composite and metal ions was vigorously shacked at 200 rpm at ambient temperature one by one. The amount of the metal ions in aliquots were determined. During kinetic studies, the metal adsorption at the composite surface was evaluated using the optimized conditions at different time intervals (0–250 min).

Results and discussion

Characterization

FTIR and FE-SEM. The FTIR spectra of GO, silica monolith, and *N*-phenyl acrylamide-modified silica-anchored GO (the resulting composite material) are given in Fig. 2 representing the corresponding functional groups.

The peaks at 1616 cm^{-1}, 3400 cm^{-1}, and a broad peak in the range of 3100 to 3500 cm^{-1} in the FTIR spectrum of GO represent various modes of OH functional groups. Similarly, the peak at 1734 cm^{-1} represents the carboxyl group, while the observed peak at 2990 cm^{-1} represents the stretching frequency of the CH_2 functional group at the surface of GO. The peak findings of the GO spectrum agree with the reported literature.[60,61] The peak at 1718 cm^{-1} shows the presence of C=O functional groups[62] while the peaks at 975–1030 cm^{-1} are affirmative of the presence of C–O–C,[63] at the surface of GO. In the FTIR spectra of monolithic silica, the observed peaks at 1112 to 1189 cm^{-1} represent the Si–O stretching frequency.[64]

The FTIR spectra of the resulting composite material (*N*-phenyl acrylamide-bound silica-anchored GO) is a clear clue for the successful synthesis of the composite, where the sharp peaks at 1081 cm^{-1} represent the stretching frequency related to the C–O functional group.[65] The vanishing of the peak for carboxyl group at 1734 cm^{-1} at the GO surface and the formation of a peak at 1380 cm^{-1} corresponding to the vibrational

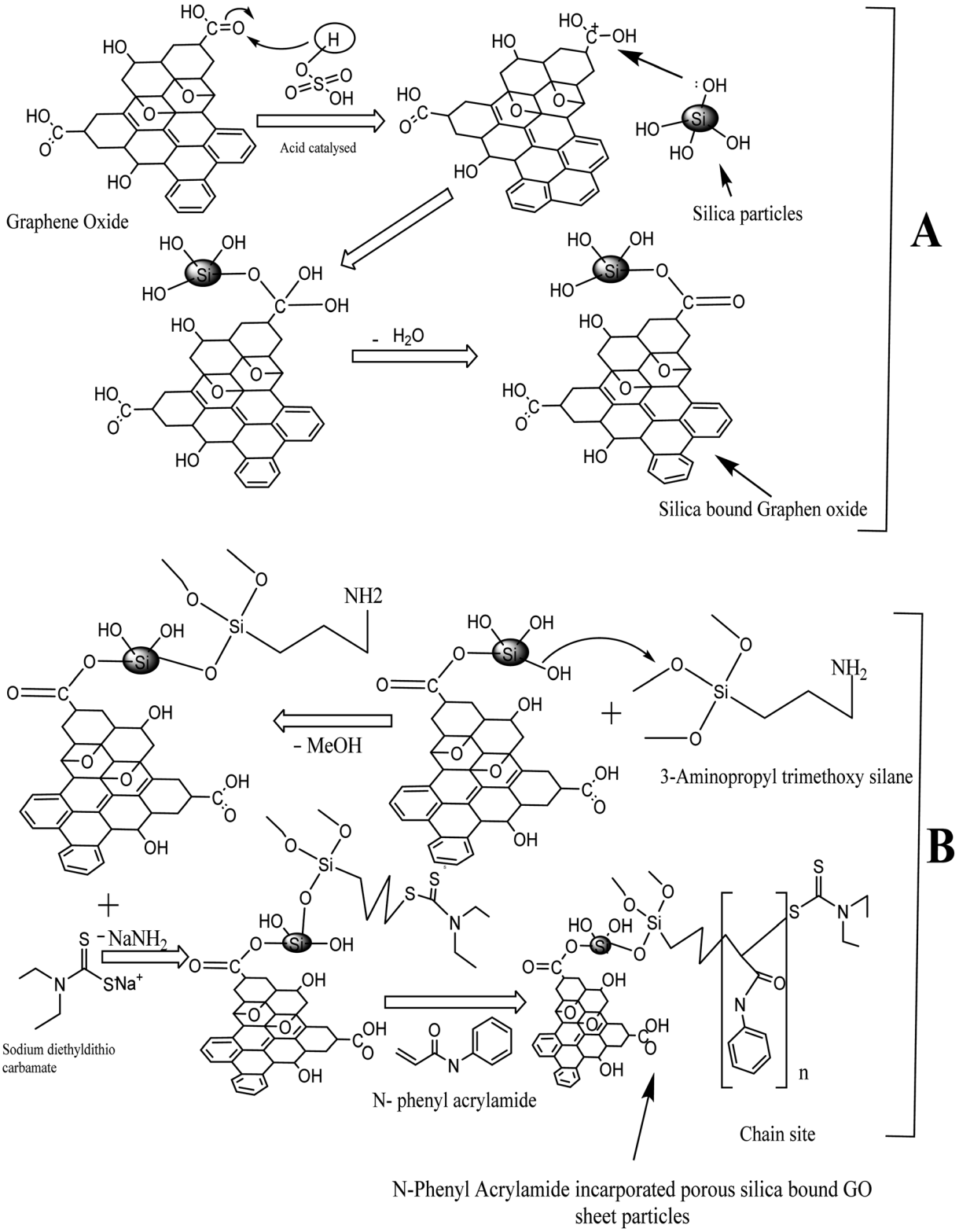

Fig. 1 Scheme of synthesis: (A) silica-bound graphene oxides and (B) *N*-phenyl acrylamide-modified silica-bound graphene oxides.

frequency of the carbonyl group bound to the siloxane (Si–O–Si) networking[66] strongly suggest the synthesis of the *N*-phenyl acrylamide-bound composite. The formation of Si–O–C=O occurs due to the reaction of the silica–OH group with the COOH group of GO, which lead to the formation of silica-bound GO particles. The peaks observed at 552 and 652 cm^{-1} in the resulting composite represent the stretching frequency of Si–O.[67] The peaks at 742 and 858 cm^{-1} represent the hydrogen

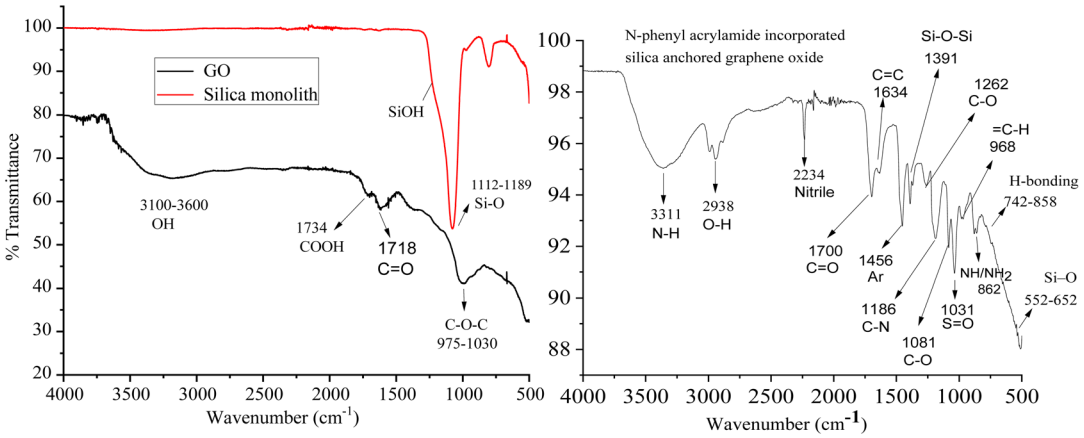

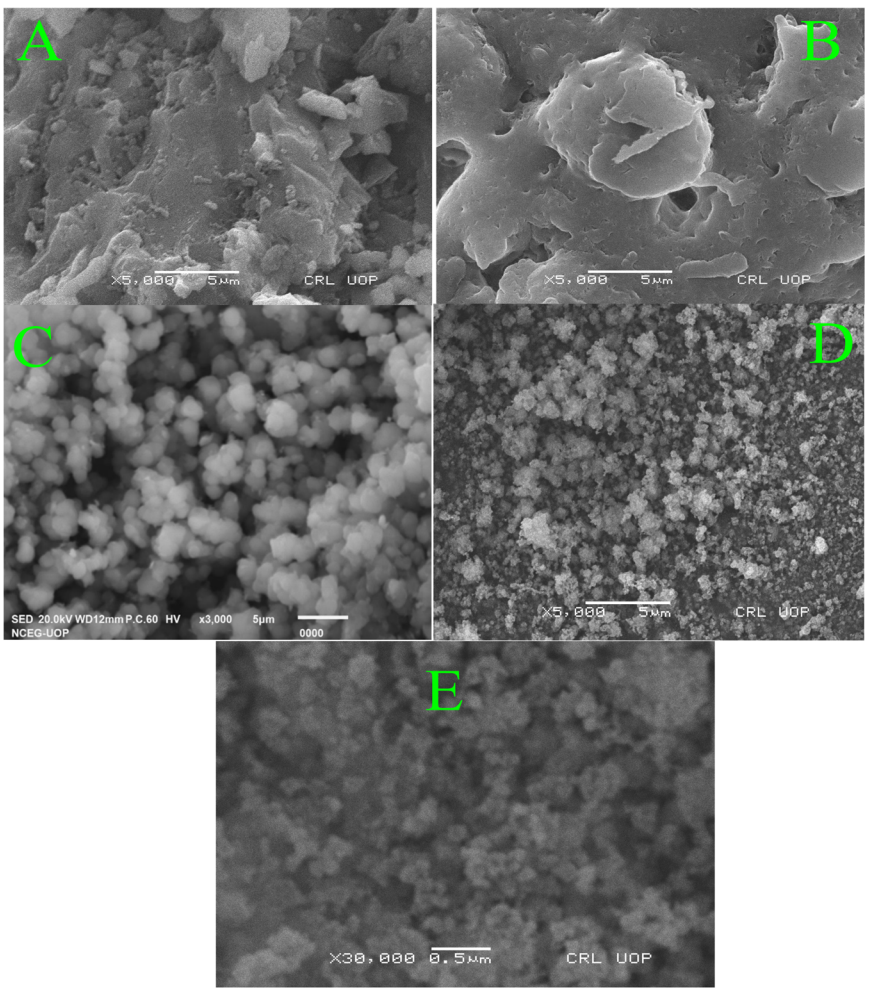

Fig. 2 FTIR spectra of the graphene oxide, silica monolith, and silica-anchored graphene oxide composite. FE-SEM images of the graphene oxide (A and B), silica monolith (C), silica-anchored GO (D), and *N*-phenyl acrylamide-incorporated silica-anchored GO (E).

bonding. The broad peak at 3311 cm^{-1} represents the NH functional group, and the overlap sharp peak at 2938 cm^{-1} is due to the OH functional group. The peak at 1700 cm^{-1} is due to the presence of C=O, and the peak at 1456 represents the presence of aromatic benzene. All the changes associated with the formation of composites from silica and GO in the form of IR spectroscopy confirm the successful synthesis of the ultimate composite material.[68]

To check the architecture and surface morphology of the GO, monolithic silica, silica-anchored GO, and *N*-phenyl acrylamide-modified composite, FE-SEM images were taken (Fig. 2). The surface morphological plan of the monolithic silica, GO with

relative variations after the deposition of monolithic silica onto the GO and the deposition of *N*-phenyl acrylamide monomers suggests the successful synthesis of the resulting composite material. The SEM images of monolithic silica indicate the particle size in the range of 1–2 μm with roughly spherical and porous nature.[69] The SEM images of the GO show sheet-like nature.[70] The SEM image of silica-incorporated graphene oxides clearly demonstrated that the small silica particles are attached to the surface of GO sheets. The silica particles overcrowd the surface of GO, which is clearer from the lumpy nature of the SEM image. The silica particles can be seen as white patches on the dark background of the GO. The SEM image of *N*-phenyl acrylamide-modified composite shows a somewhat synchronized image where the entire surface is modified with the polymer layer.

X-ray diffraction analysis. The XRD plot for GO with diffraction line (d-spacing 0.34, 001, nm at 26.05°) represents the partial oxidation of GO,[71] as depicted in Fig. 3. A special peak at 10.99° (*d*-spacing between sheets of 0.81 nm) in the XRD image of GO represent the hexagonal structure of carbon sheets forming the GO;[72] besides, the sharp peak shows the crystalline nature of graphene and graphene oxide sheets.[73] Such results were also observed for the GO sheets prepared *via* Hummer' method.[74] An intense broad peak was observed at 20°–23° in the XRD image of monolithic silica corresponding to the OH, Si–OH functionalities, and amorphous nature of the silica particles according to Fig. 3.[75]

The XRD image of the composite confirms the presence of both monolithic silica and GO. The intense peaks observed at diffraction 2θ = 0.4–2.4° up to 100–200 represent the well-ordered two-dimensional hexagonal structure of GO sheets in the composite,[76] while the broad silica peak was seen at 20°–23° and those of the GO were observed at 11 and 26°. A slight shift in the (0.002) maximum peaks from 26.05° to 26.20° was observed in the XRD image of composites, which might be attributed to the reduction of GO.[77] The XRD results agree with the successful formation of the composite.

Pore size and surface area *via* BET/BJH analysis. The pore size distribution of the GO, silica monolith, silica-bound GO, and polymer-modified silica-bound GO was analysed by the BET/BJH analysis by the adsorption–desorption isotherm using the nitrogen gas (Fig. 4). The isotherm linear plots indicated that the composite is microporous having a pore size of 57 nm. The resulting composite possesses a specific surface area of 264.899 $m^2\ g^{-1}$, a pore volume of 0.51009 $cm^3\ g^{-1}$, and a pore radius of 26.5 nm (Table 2).

The pore radius of the GO is 28.5 nm, silica monolith is 18 nm, silica bound GO is 16.5 nm, and that of the polymer-bound composite is 13.5 nm. A decrease in the pore radius of silica bound GO is due to the deposition/growth of silica particles over the GO sheets. Similarly, a further decrease in the pore radius to 13.5 nm for the polymer-bound composite is due to the immobilization of the polymer film over the composite surface. The RAFT polymerization results in polymer formation, leading to decreased pore size. The pore size distribution analysis is a clue towards the successful synthesis of the resulting composite material. The porosity

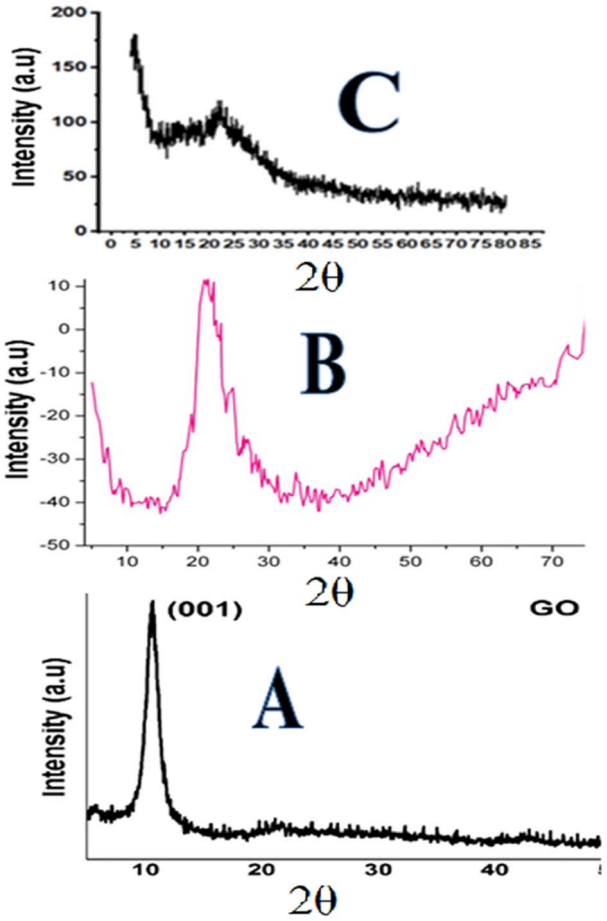

Fig. 3 XRD pattern: (A) graphene oxide, (B) silica particles and (C) phenyl acrylamide-incorporated porous silica-bound graphene oxide sheets.

indicates the ratio of the open pore volume to that of the total volume of the composite.[78] The high surface area and porosity are very significant for the enhanced adsorption of adsorbent materials.[79] The higher total pore volume of 21–25 nm materials confirms its mesoporous nature.[80] The numerical values of the BET/BJH analysis for the *N*-phenyl acrylamide-modified composite are summarized in Table 2.

Nature and magnitude of charges on composite materials (the zeta potential). The nature and magnitude of charges at the interfacial layer of the dispersed composite material were found out by the zeta potential.[81] The negative functional groups at the surface of GO sheets were generated during the oxidation process, which corresponds to the negative zeta potential. The higher oxidation density of GO results in a large density of the functional groups at the GO surface corresponding to the increase in zeta potential value even further. Many of the oxygen-containing functional groups of a higher zeta potential in a solution are due to the dissociation of many acidic functional groups such as ($COOH \rightarrow COO^- + H^+$) at the surface of the materials. The ASTM explains the stability of materials in the suspension form in terms of zeta potential values. Materials, with a zeta potential < 30 mV

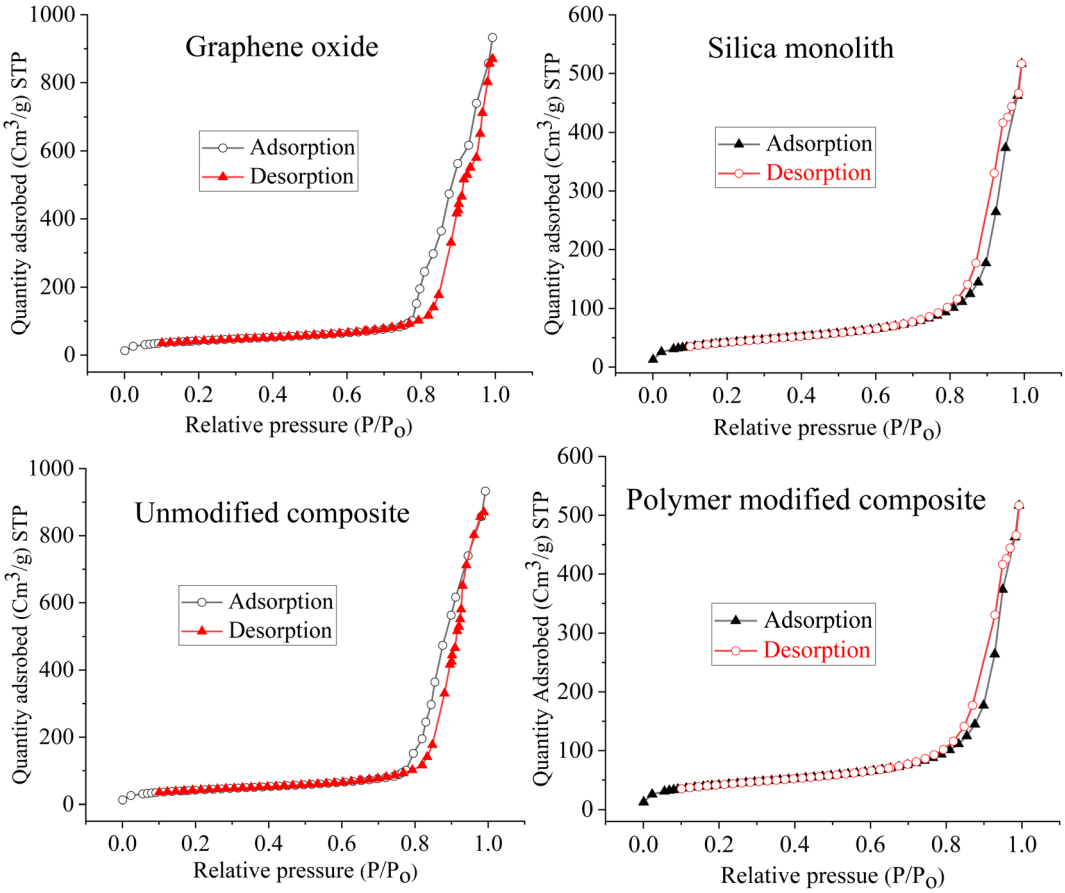

Fig. 4 Adsorption–desorption isotherm linear plots for the pore size of the graphene oxide, silica monolith, silica-anchored graphene oxide, and *N*-phenyl acrylamide polymer-bound silica-anchored graphene oxide composite which are 570 Å, 360 Å, 330 Å, and 270 Å respectively.

Table 2 Summary report of the pore size, pore volume, and surface area of silica modified GO demonstrated *via* BET/BJH analysis

	Reaction conditions/descriptions	Results
Surface area ($m^2\ g^{-1}$)	Single point surface area at $P/P_0 = 0.199472855$	264.899 ($m^2\ g^{-1}$)
	BET surface area	259.799 ($m^2\ g^{-1}$)
	t-Plot micropore Area	15.589 ($m^2\ g^{-1}$)
	t-Plot external surface Area	261.687 ($m^2\ g^{-1}$)
	BJH adsorption cumulative surface area of pores between 17.000 Å and 3000.000 Å diameter	259.389 ($m^2\ g^{-1}$)
	BJH desorption cumulative surface area of pores between 17.000 Å and 3000.000 Å diameter	291.243 ($m^2\ g^{-1}$)
Pore volume (Cm^3/g)	Single point adsorption total pore volume of pores less than 2566.419 Å diameter at $P/P_0 = 0.992420088$	0.51009 ($cm^3\ g^{-1}$)
	t-Plot micropore volume	0.00238 ($cm^3\ g^{-1}$)
	BJH adsorption cumulative volume of pores between 17.000 Å and 3000.000 Å diameter	0.49226 ($cm^3\ g^{-1}$)
	BJH desorption cumulative volume of pores between 17.000 Å and 3000.000 Å diameter	0.51009 ($cm^3\ g^{-1}$)
Pore size (Å)	Adsorption average pore width (4 V/A by BET)	227.920 (Å)
	BJH adsorption average pore diameter (4 V/A)	244.927 (Å)
	BJH desorption average pore diameter (4 V/A)	221.391 (Å)

(either negative or positive), are less stable, with a zeta potential > 40 mV are highly stable, and with a zeta potential between 30 and 40 mV are moderately stable.[82] The peak at a zeta potential of −12.52 mV corresponds to the COOH, epoxy, and OH functional groups at the surface of GO, suggesting the unstable nature of the GO.

The monolithic silica shows zeta potentials of −38.4 mV and −9.9 mV, which are related to the silanol functional groups.

The overall zeta potential of −48.3 mV of the silica monolith suggests a higher silanol density at the surface and increased stability of the silica particles. The nutshell zeta potential on the surface of the composite is −21.18 mV. The peak at −30.9 mV in the zeta potential plot of the polymeric materials is typically due to the esterification reaction between COOH and Si–OH groups, while the peaks at 2.4 mV and 13.4 mV might be due to the epoxy and hydroxyl functional groups. The numerical values of zeta potential are summarized in Table 3. The zeta potential analysis suggests the improved removal efficiency of Cr(VI)and Cr(III) at the optimized pH owing to the highly negative surface of the resulting composite. In addition, the zeta potential is a clue for the successful synthesis of the *N*-phenyl acrylamide-modified silica@GO. Besides the electrostatic interaction, the presence of the hydroxyl group at the surface of silica and epoxy, carboxyl, and phenolic OH at the GO surface results in hydrogen bonding and van der Waals forces during the adsorption process.[83] Moreover, the incorporation of the *N*-phenyl acrylamide in the resultant composite might result in the enhanced interaction between Cr and the composite, leading to highly efficient adsorption of the former.

Table 3 Values of zeta potential for GO, silica monolith and polymer modified silica bound GO composite

S. No.	Samples	Zeta potential (mV)
1	GO	−12.52
2	Silica monolith	−48.3
3	Silica anchored GO composite	−21.18

Energy-dispersive X-ray analysis of the composite before and after the adsorption of Cr(VI) and Cr(III). The energy-dispersive X-ray analysis (EDX) of the resulting polymer-bound composite material was carried out before and after the adsorption of Cr(VI) and Cr(III) (Fig. 5). The EDX plots showed peaks for Cr(VI) and Cr(III) after the analytes were adsorbed at the composite surface. The EDX images before adsorption contain C ∼ 78%, silica ∼ 46.6%, sulphur ∼ 3.8%, nitrogen ∼ 30.80%, oxygen ∼ 19%, and Cl ∼ 0.4%. After the adsorption of Cr(VI), the related concentrations computed from the area under the corresponding peaks were decreased, C ∼ 75%. The relative amount of Cr(VI) is about 5%, oxygen ∼ 12.5%. Cr(VI) was successfully adsorbed at the composite surface. The findings of the current study are in accordance with ref. 84. Similarly, after the adsorption of Cr(III), a peak of about 2.97% appeared in the EDX spectrum along with the presence of C, N, O, Si, and S with somewhat diminished peak intensities.[85]

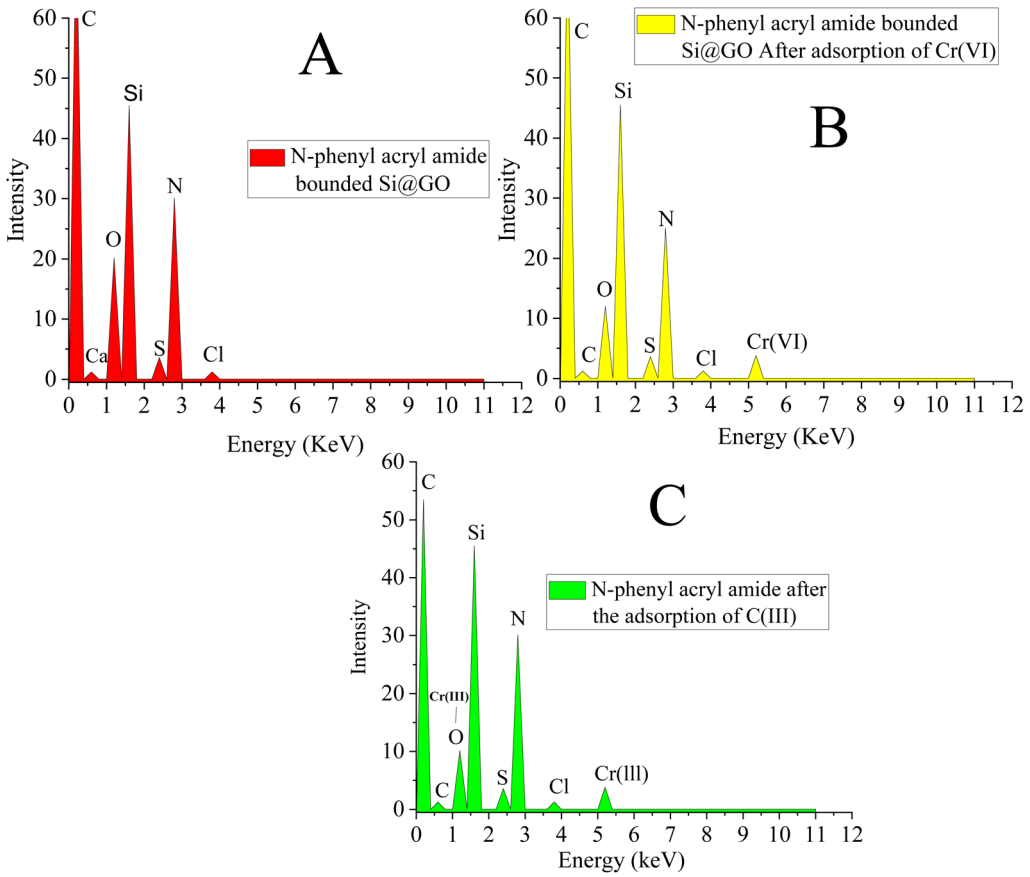

Fig. 5 EDX images of the polymer-bound silica-anchored graphene oxide: (A) before adsorption, (B) after adsorption of Cr(VI) and (C) after adsorption of Cr(III).

Batch adsorption/optimization studies. Cr(VI)and Cr(III) adsorption on the surface of the resulting adsorbent was demonstrated and the amount of the metal ions in the filtrate were calculated by atomic absorption spectrometry. The optimum conditions affecting the adsorption of Cr(III) and Cr(VI) were optimized.

Adsorption mechanism between the composite and the analyte.

The Cr(VI) which exists in the form of $HCrO_4^{2-}$ in acidic media (pH 2) is reduced by the OH group of GO into the Cr(III) ion, which is adsorbed at the chain propagation sites of the polymers or by the electrostatic interaction with oxygen, as

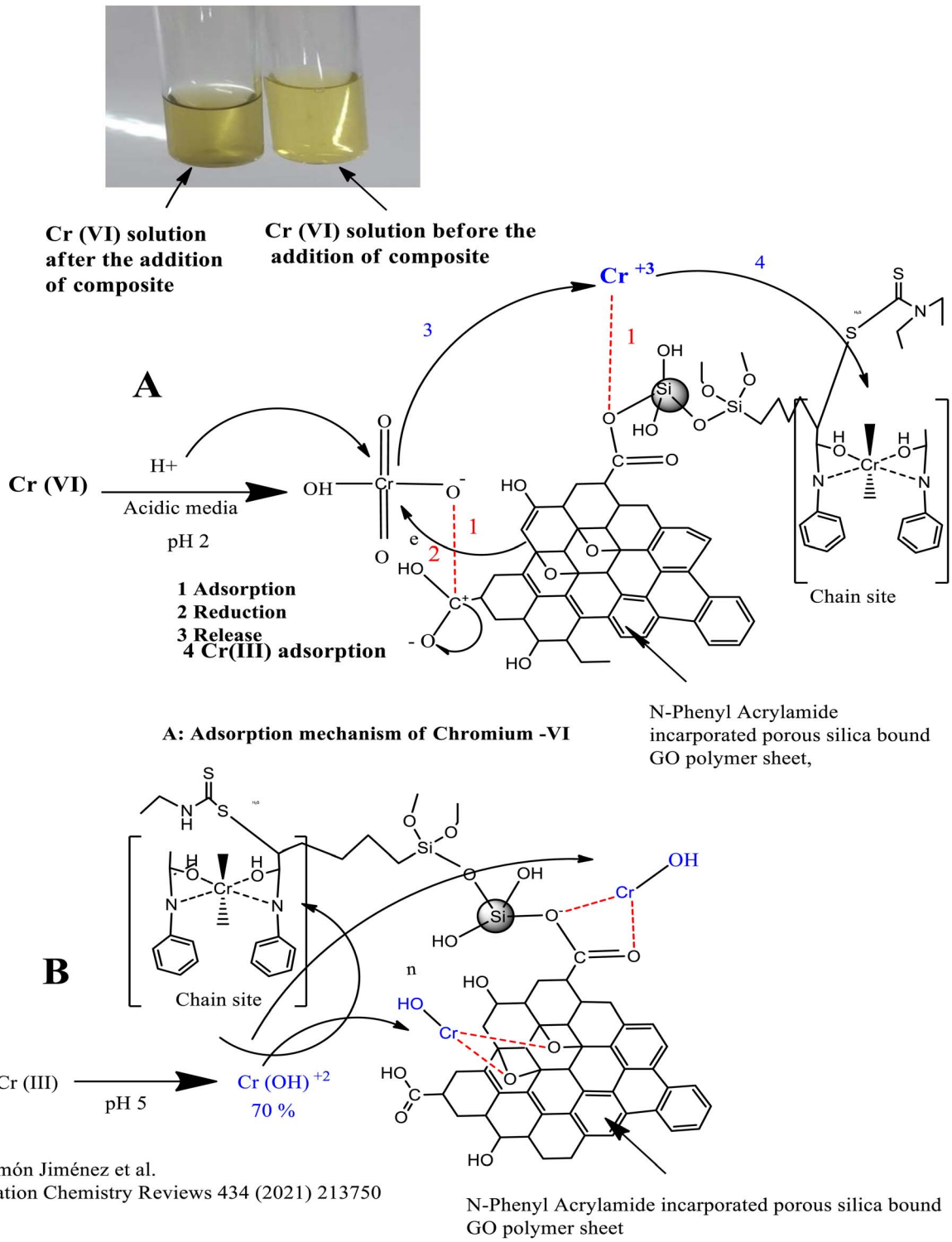

Fig. 6 Scheme for the adsorption of (A) chromium(VI) and (B) chromium(III).

shown in Fig. 6(A). Similarly, Cr(III) which exists in the form of $Cr(OH)_2^+$ at pH 5 is adsorbed either directly at the chain propagation sites of the polymers or by the electrostatic interaction with the oxygen of the GO sheets, as shown in Fig. 6(B).

pH effect. During the adsorption of Cr(III) and Cr(VI) at the surface of the polymer-modified composite materials, the effect of pH was found to be a critical parameter. A series of pH solutions from (2–11) were tried for finding the optimum value using an adsorbent amount of 3 mg and an adsorbate concentration of 20 mg L^{-1} in 25 mL volume with a shaking time of 30 min for both metal ions. Maximum adsorption of 96.64% was recorded at pH 2 for Cr(VI) and 96.5% was observed for Cr(III) at pH 5. A decrease in the percentage of adsorption was recorded in basic media. The computed zeta potential of the polymer (−9.18) indicated that the whole surface of the polymer must be negative at pH values less than 9.18. In acidic media, the hydrogen ion deposits at the polymer surface by making bonds with surface silanol groups. It renders the whole surface positive owing to the formation of hydronium ions. Cr(VI) exists in the form of $HCrO_4^{2-}$ in the pH range of 1 to 6. At pH 2, H^+ reduces Cr(VI) by accepting electrons from the OH or C=O functional groups of the GO. Cr(VI) might also reduce to Cr(III), resulting in the colour change from yellow to green. Cr(III) might be attracted by the oxygen containing functional group of the adsorbent by electrostatic interaction or take part in complex formation with the donor groups (N, C=O) of the polymers, as depicted in Fig. 6(A) and it might enhance the adsorption.

In the basic media, there exists a competition for the adsorption of OH^- and $HCrO_4^{2-}$ ions on the adsorbent surface, which lowers the percentage of adsorption of the Cr-metal. Furthermore, a decrease in percentage of adsorption of Cr(VI) in basic media might be attributed to the repulsion between OH^- and HCO_4^{2-}.[86]

Similarly, the adsorption of Cr(III) is maximum at pH 5, where 70% of Cr(III) exist in the form of $Cr(OH)_2^+$, which form a complex with oxygen- and nitrogen-containing functional groups of the polymer-bound composite or hydrogen bond,[87] as shown in Fig. 6(B). The decrease in the percentage of adsorption at lower pH values may either be attributed to the excess of hydrogen ions or the precipitation of Cr-III in the form of $Cr(OH)_3$, which usually occurs at pH 4.[88,89] A slightly less increase was observed in the percentage of adsorption in a basic medium due to the dissociation of (Si–OH) groups into the Si–O–, and adsorbate–adsorbent hydrogen bonding interactions.[90] The pH effect is given in Fig. 7.

Adsorbent dose. The adsorption ability of the polymer-modified composite towards Cr(III) and Cr(VI) was computed at different adsorbent concentrations. A gradual increase was noticed in the adsorption of Cr(III) and Cr(VI) by increasing the adsorbent concentration from 2 to 10 mg, keeping all other conditions constant. The computed maximum adsorption

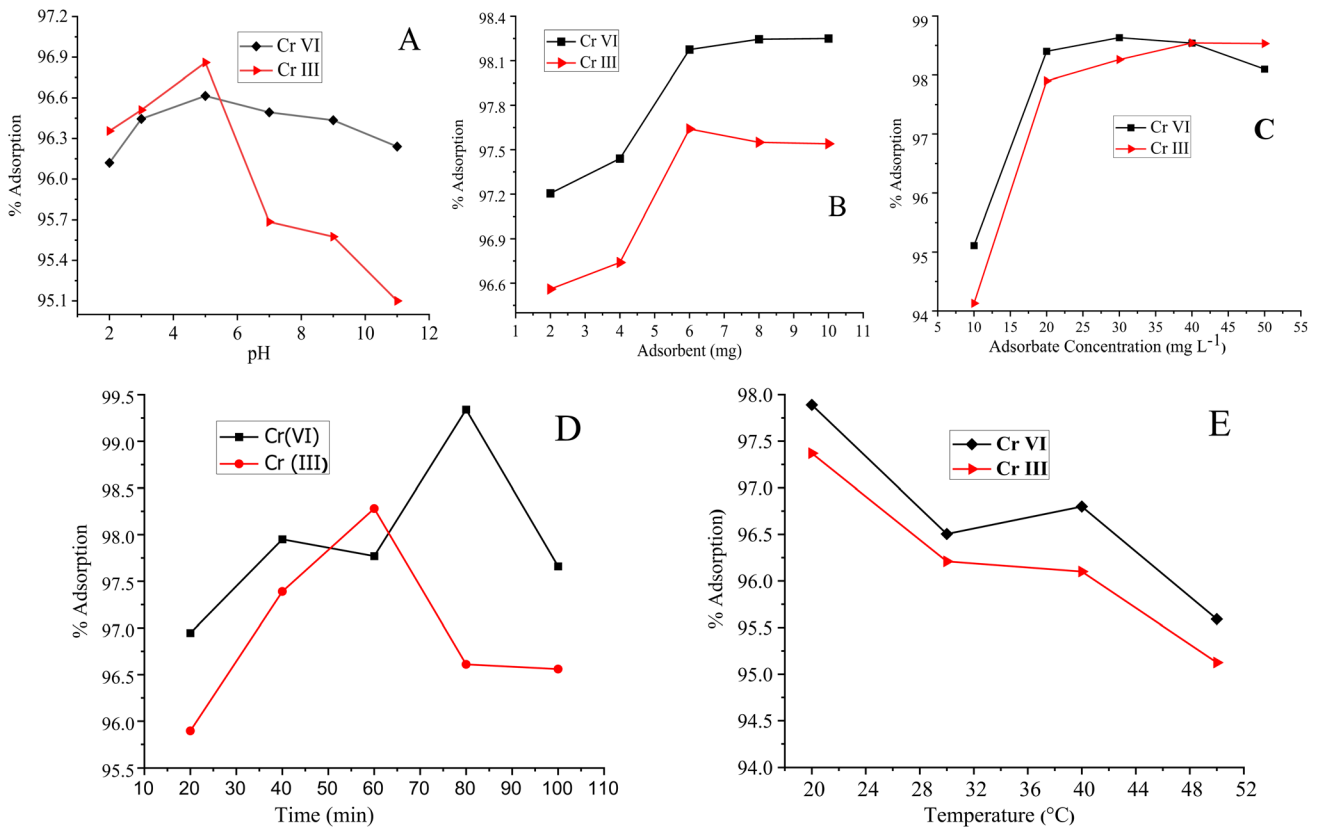

Fig. 7 Plots for the effect of (A) pH, (B) adsorbent dose, (C) adsorbate amount, (D) shaking time, and (E) temperature on the adsorption of Cr-VI and Cr-III onto the silica-bound graphene oxide.

(98.245%) of Cr(VI) was noticed using 8 mg of the adsorbent at pH 2, an adsorbate concentration of 20 mg L^{-1}, a contact time of 60 min, and a solution volume of 10 mL using the ambient temperature, as shown in Fig. 7(B). Similarly, for Cr(III), the maximum adsorption (97.64%) was noticed at an adsorbent dose of 6 mg, while keeping other conditions constant such as pH 6, an adsorbate concentration of 20 mg L^{-1}, a contact time of 60 min, and a solution volume of 10 mL at room temperature. The percentage of adsorption initially increases for both metal ions by increasing the adsorbent dose and becomes constant after reaching a certain percentage of adsorption. The observed constant percentage of adsorption beyond 8 mg for Cr(VI) and 6 mg for Cr(III) is due to the saturation of adsorbent sites.[91–93]

Amount of the adsorbate. The adsorptive capacity of the polymer-bound composite material towards Cr(VI) and Cr(III) were found to be different at different concentrations of the Cr metal ions. A series of Cr(VI) and Cr(III) solutions were prepared in the range of 10 to 50 mg L^{-1} using K_2CrO_4 and $CrCl_3$ keeping other parameters constant. The observed maximum adsorption of Cr(VI) (98.63%) was observed at 30 mg L^{-1} of the adsorbate solution at pH 2, an adsorbent dose of 8 mg, a contact time of 60 min, a volume of 10 mL, at ambient temperature. Similarly, the documented maximum adsorption of Cr(III) (98.83%) was observed using 40 mg L^{-1} of the adsorbate at pH 6, an adsorbent amount of 6 mg, a contact time of 60 min and at room temperature. The linear increase in the percentage of adsorption of both metal ions with adsorbate concentration is due to the availability of more active sites at the polymer surface. Declination in both curves after the optimum percentage of adsorption is due to the saturation of active sites on the polymer surface since most of the binding sites were occupied by the adsorbate molecules.[94] At an elevated concentration of Cr(VI), a slight increase in the percentage of adsorption is due to particle diffusion (adsorbate diffusion into the composite pores) and film diffusion (adsorbate diffusion from the exterior to the interior surface of the polymer).[95,96]

Cr(VI) demonstrated the maximum adsorption (98.63%) at an adsorbate concentration of 30 mg L^{-1}. Initially, the percentage of adsorption of Cr(VI) was 95.11%, which then linearly increased to 98.63%, as shown in Fig. 7(C). Similarly, the Cr(III) adsorption was linearly increased to 98.832% and then became constant. The observed linear increase in the percentage of adsorption of the metal ions with metal concentration is because of the more active sites available at the adsorbent surface. The adsorbate–adsorbent interactions are higher at elevated adsorbate concentrations owing to the improved mass transfer effects, which ultimately increase the driving force.[97]

Shaking/contact time. A series of (20 mg L^{-1}) five solutions of Cr(VI) and Cr(III) were prepared in 25 mL volumetric flasks. All the solutions of both states of the Cr-metal were subjected to different shaking times (20–100 min) at ambient temperature.

The Cr(VI) adsorption increases linearly from 10 to 80 min and then a decrease was observed. Similarly, the Cr(III) adsorption was increased with extra shaking time. Maximum adsorption for Cr(III) was found to be 98.28% at 60 min. The higher shaking time suggests low mass transfer kinetics of the process since this is the time required for exposing the entire active sites of the adsorbent to the metal ions. Finally, the active sites are all done with the adsorption of the metal ions in solutions and the percentage of adsorption adopts the pattern given in Fig. 7(D).[98] The time at which maximum adsorption is achieved is the time required for the attainment of equilibrium between metal ions and the adsorbent material in each solution.[99]

Temperature. Finally, the temperature effect was studied on the adsorption of the metal ions on the adsorbent material. A series of Cr(III) and Cr(VI) solutions were prepared, and a different temperature was applied to the solutions (30 to 60 °C), as shown in Fig. 7(E). The maximum adsorption of Cr(VI) was found to be 97.895% at 20 °C and that of Cr(III) was found to be 97.375% at 20 °C. A decrease in the percentage of adsorption of both states of the Cr-metal by increasing the temperature suggests the exothermic processes.[100]

Isotherm study. The adsorption isotherm/models were applied to the adsorption data of Cr(III) and Cr(VI) at the surface of the adsorbent for illustrating their equilibrium concentration. At equilibrium, the adsorption data of Cr-metal ions was analysed through Langmuir, Freundlich, and Temkin models.[101,102]

Langmuir adsorption isotherm model illustrated the monolayer/uniform adsorption at the adsorbent surface having an inadequate number of active sites. The q_e value in the Langmuir adsorption isotherm model represents the monolayer adsorption. The q_e value for Cr(III) and Cr(VI) are 298.507 mg g^{-1} and 114.810 mg g^{-1} respectively. The adsorption constant (K_L in L mg^{-1}) in the Langmuir model represents the adsorption affinity of the adsorbate in a bulk solution to the active sites. The K_L value for Cr(VI) and Cr(III) was found to be 0.7923 L mg^{-1} and 0.9101 L mg^{-1} respectively.[103]

Freundlich adsorption isotherm model is usually applied to signify the analyte adsorption at the non-uniform and heterogeneous surface of the adsorbent.[104] The K_F (mg g^{-1}) is the Freundlich adsorption constant representing the adsorption capacity. The K_F values for Cr(III) and Cr(VI) were found to be 138.653 mg g^{-1} and 401.874 mg g^{-1} respectively. The Freundlich parameter "$1/n$" is the sorption and heterogeneous factor, where ($n > 1$ or $1/n < 1$) represent the favourability of metal adsorption at the composite surface. The $1/n$ value was computed as 0.809 for Cr(VI) and 2.027 for Cr(III).[105]

The R^2 (0.972) computed from the Langmuir adsorption isotherm for Cr(VI) best fits to its adsorption at the composite surface, as shown in Fig. 8. The R^2 (0.983) value for Cr(III) given in Table 4 is computed from the Freundlich adsorption isotherm, suggesting best fitting of the adsorption data to the Freundlich model.

The Langmuir adsorption isotherm for Cr(VI) indicated that the adsorption of Cr(VI) (which exists in the form of $HCrO_4^{2-}$) at the surface of the *N*-phenyl acrylamide-bound composite is monolayer and chemisorption. During this process, Cr(VI) is reduced to Cr(III) by the OH group of GO sheets, which further bind electrostatically with an oxygen atom or may form a complex with a polymer chain at the propagation sites, as shown in Fig. 6(A). The adsorption data of Cr(III) follow the Freundlich adsorption isotherm because Cr(III) at pH 5 exists in

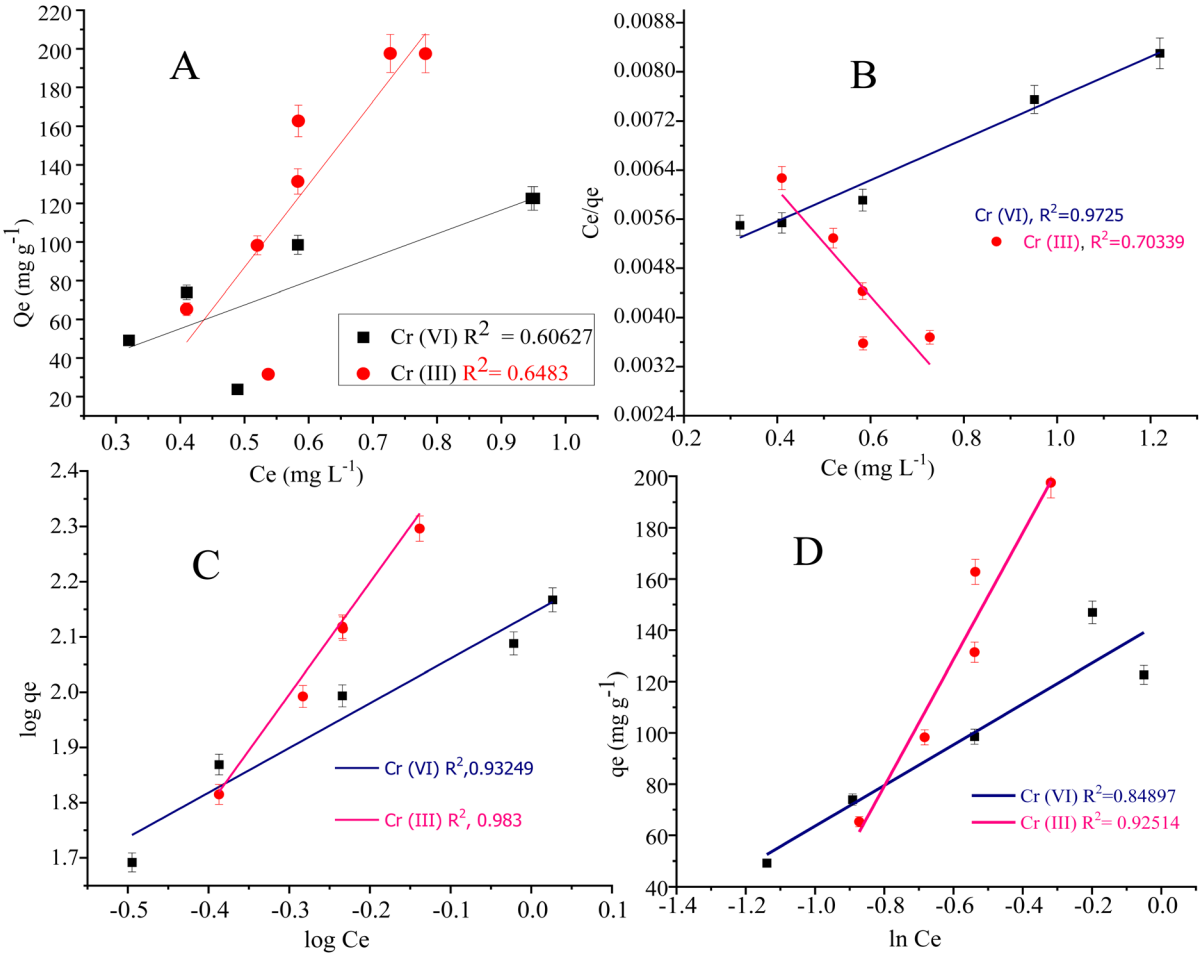

Fig. 8 Isotherm models: (A) adsorption isotherm, (B) Langmuir adsorption isotherm, (C) Freundlich adsorption isotherm, and (D) Temkin adsorption isotherm for the adsorption of chromium-VI and III metals.

Table 4 The isotherm models and values of the calculated parameters for the adsorption of Cr(VI) and Cr(III) on silica anchored GO composite

Isotherm model	Langmuir model			Fruindlich model				Temkin model		
Linear equation	$C_e/q_e = 1/K_L Q_m + C_e/Q_m$			$\log q_e = \log K_F + \frac{1}{n}\log C_e$				$Q_e = B \ln A + B \ln C_e$		
Parameters	K_L (L g^{-1})	q_e (mg g^{-1})	R^2	K_F (mg g^{-1})	N	$1/n$	R^2	A	B (J mol^{-1})	R^2
Chromium(VI)	0.7923	298.507	0.972	138.653	1.235	0.809	0.9324	1.2339	79.523	0.848
Chromium(III)	0.9101	114.810	0.946	401.874	0.4933	2.027	0.983	8.0352	247.1717	0.925

the form of $Cr(OH)_2$ + 2. The $Cr(OH)_2^{2+}$ show physisorption at the composite surface and is more prominently the electrostatic interaction. The binding is mainly due to the formation of hydrogen bonds with nitrogen or oxygen functional groups of the adsorbent, as shown in Fig. 6(B). The Temkin isotherm model was also applied to the adsorption data of Cr(VI) and Cr(III). The Temkin constant (B) represent the adsorption heat in the unit of J mol^{-1} while "R" is the gas constant (8.314 J mol^{-1} K^{-1}), "A" is the Temkin constant and "T" is the temperature in Kelvin.[106] The constant values B and A were calculated from the slope and intercept of the plot of q_e *vs.* $\ln C_e$, as shown in Fig. 8(D).

Kinetic studies. The kinetic studies demonstrated the rate controlling step and adsorption mechanism of Cr(III) and Cr(VI) at the composite surface. A series of different solutions of the chromium salt of both oxidation states (VI and III) were prepared and the adsorbent addition was carried out at different time intervals (20–100 min). The adsorption data of Cr(VI) and Cr(III) from the bulk solution at the adsorbent surface at different time spans were used in the kinetic studies. Pseudo 1st, 2nd and intra particle diffusion kinetic

models were applied to the data, which are summarized in Table 5 and Fig. 9.

The linear form of the kinetic models (pseudo first-order eqn (3), pseudo second-order eqn (4), and intraparticle diffusion eqn (5)) was applied to the adsorption data of Cr(III) and Cr(VI):

$$\log(q_e - q_t) = \log\ q_e - k_1 \frac{t}{2.303} \quad (3)$$

$$\frac{t}{q_t} = \frac{1}{k_2 q_e^2} + \frac{t}{q_e} \quad (4)$$

$$q_t = k_{id} t^{1/2} + C \quad (5)$$

where k_1 (min^{-1}), k^2 (mg^{-1} min^{-1}), and k_{id} (mg^{-1} min^{-1}) are the relative rate constants for the pseudo first order, pseudo second order, and intraparticle diffusion models respectively. q_t (mg g^{-1}) is the amount of metal adsorbed at time (t), and q_e (mg g^{-1}) is the adsorbed amount of the metal after attainment of the equilibrium.[107] The plots of kinetic models are shown in Fig. 9 for both states of the metal ion. The relative parameters computed from the kinetic models of both states of the Cr-metal are summarized in Table 5. The values of q_e and k_1 for the pseudo first-order model were calculated from the intercept and slope of the curve of $\log(q_e - q_t)$ *vs.* time. The values of k_2 and q_e for the pseudo 2nd order kinetic model were calculated from the intercept and slope of the curve t/q_t *vs.* time. Similarly, the values of q_e and k_2 for the Temkin model were determined

Table 5 Adsorption kinetic study of chromium-VI and chromium-III metal ions at silica-bound graphene oxide composite material

	Pseudo 1st order kinetic				Pseudo 2nd order kinetic				Intra particle diffusion		
Metal ions	K_1 (min^{-1})	Q_e (mg g^{-1}) (calcu.)	q_e (mg g^{-1}) (exp.)	R^2	K_2 (min^{-1})	Q_e (mg g^{-1}) (calcu.)	q_e (mg g^{-1}) (exp.)	R^2	k_{id} (min^{-1}/2)	C (mg g^{-1})	R^2
Cr-VI	0.00091	94.045	146.95	0.848	3.120	47.98	146.95	0.996	0.18904	46.989	0.048
Cr-III	0.00022	130.436	197.57	0.560	3.958	64.391	197.57	0.999	0.2681	62.895	0.344

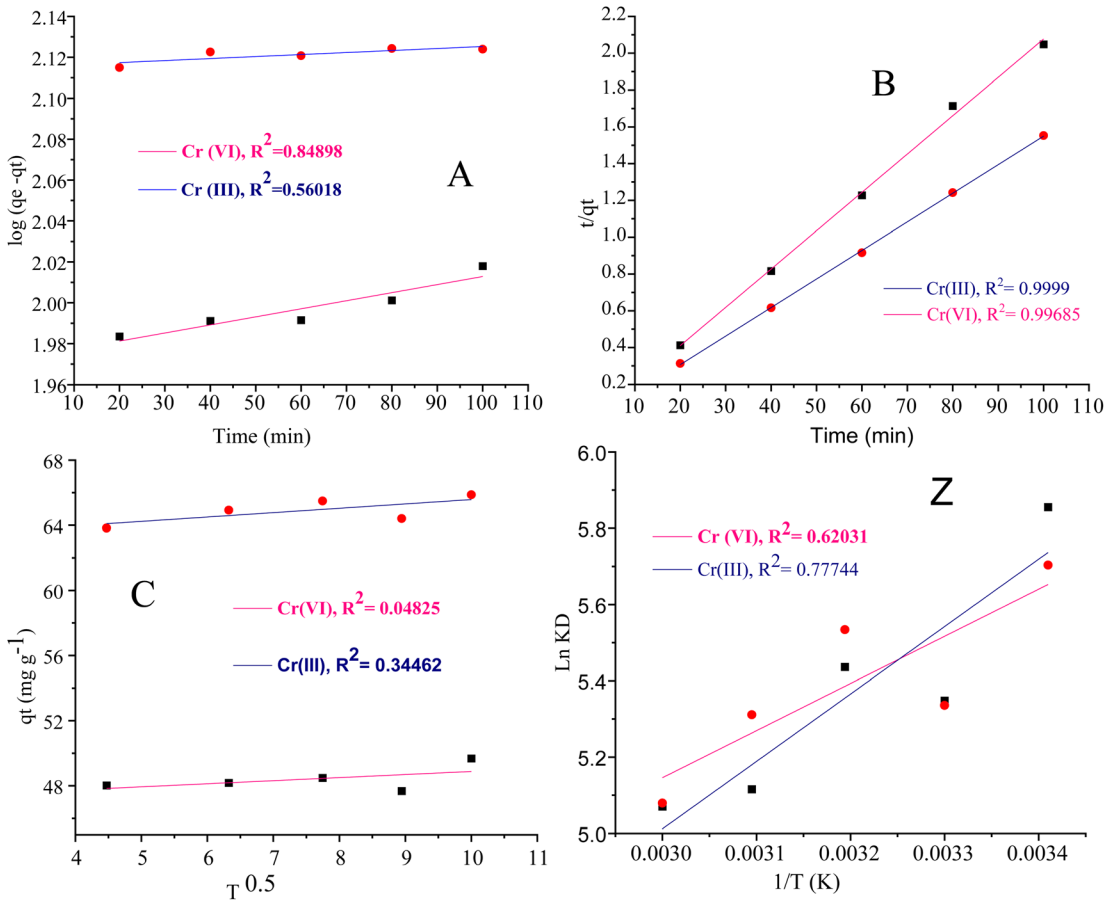

Fig. 9 (A) Pseudo first-order kinetic model, (B) pseudo second-order kinetic model, (C) intraparticle diffusion model, and the van't Hoff plot: *Z* for the adsorption of chromium-VI and chromium-III metal ions.

from the slope and intercept of the plot (t/q_t) against time at different temperatures, as shown in Fig. 9(B).

The intra particle diffusion explains the different stages of kinetics during the adsorption process, where a curve of q_t against $T^{0.5}$ was plotted, as shown in Fig. 9(C). In the first stage, the adsorbate diffusion is fast which becomes slow in the second stage and decreases further in the third stage.[108] The regression values for Cr(VI) ~ 0.996 and Cr(III) ~ 0.999 computed from the pseudo 2nd-order model suggested more applicability of the pseudo second-order model in comparison to the pseudo 1st-order model, where the R^2 values are 0.848 for Cr(VI) and 0.560 for Cr(III). The regression values computed from the intra particle diffusion model are 0.048 for Cr(VI) and 0.344 for Cr(III). The higher R^2 value suggested that the adsorption of Cr(III) and Cr(VI) at the composite surface follows pseudo 2nd order and the process is physisorption.[109]

Equilibrium and thermodynamic studies. Equilibrium and thermodynamic parameters such as change in enthalpy, entropy, and Gibbs free energy were calculated to determine the feasibility for the occurrence of the metal ion interaction with the composite. The results indicated the spontaneous occurrence of the process. The thermodynamic parameters (ΔS, ΔH and ΔG) were calculated using the following equations:

$$\Delta G = -RT \ln K_D \tag{6}$$

$$K_D = q_e/C_e$$

$$\ln K_D = -\frac{\Delta G}{RT} = -\frac{\Delta H}{RT} + \frac{\Delta S}{R} \tag{7}$$

where q_e (mg g^{-1}) is the adsorbed amount, C_e (mg L^{-1}) denotes the equilibrium concentration of both states of the metal ion and K_D is the distribution constant. The value of K_D was determined in terms of Langmuir constant (K_L) in L mol^{-1}. For the calculation of K_L in L mol^{-1}, Langmuir eqn (8) was applied.

$$Q_e = Q_{max} C_e K_L / C_e K_L + 1 \tag{8}$$

where Q_{max} and Q_e represent the maximum adsorption capacities of the composite at equilibrium in mg g^{-1}. K_L is the Langmuir constant in L mol^{-1} and C_e is the adsorbate concentration in the bulk solution. According to Langmuir, the thermodynamic equilibrium is given as follows:

$$K_a = \partial_a/((1 - \partial_e)a_e \tag{9}$$

and

$$a_e = \gamma_e C_e / C_s \tag{10}$$

a_e is the activity of adsorbate in the solution at equilibrium and ∂_e is the fraction of the covered surface.

γ_e is the activity co-efficient at equilibrium and C_s is the molar concentration of adsorbate present in the reference standard solution, which is equal to 1 mol L^{-1}.

Then, eqn (11) becomes

$$K_a = \partial_a/((1 - \partial_e)\gamma_e C_e \tag{11}$$

$$\partial_e = Q_e/Q_{max}$$

Putting this value in eqn (8), we get eqn (12) as follows:

$$K_L = \theta_e/(1 - \theta_e)C_e \tag{12}$$

By comparing eqn (11) and (12), we get

$$K_a = K_l/\gamma_e \text{ 1 mol } L^{-1} \tag{13}$$

γ_e represents the function of ionic strength of the solute.

For a very dilute solution or weak charges adsorbate $K_a = K_L$. Eqn (6) will become

$$\Delta G = -RT \ln K_L \tag{14}$$

For the dilute solution of Cr(VI) and Cr(III), we applied the Langmuir constant K_L instead of K_D.

The van't Hoff plot $\ln K_L$ *vs.* $1/T$ given in Fig. 9(Z) was constructed for Cr(VI) and Cr(III).

According to Milonjic *et al.*, $\Delta G°$ can be calculated using the value of K_L if adsorption takes place in an aqueous solution. Under such conditions, K_L should be converted into a dimensionless constant by multiplying with 55.5 mol L^{-1}. The 55.5 value can be calculated by dividing 1000 g by the molar weight of water, and the $\Delta G°$ value can be calculated according to eqn (15):

$$\Delta G° = RT \ln(55.5\ K_L) \tag{15}$$

According to this equation, the substance activity is the ratio of the substance's concentration to that of the reference (1 mol L^{-1}); therefore, the concentration units in the ratio cancelled each other out where the activity is dimensionless. Therefore, the equation is against the chemical activity concept.[110]

The negative values of ΔH (−12.193 kJ mol^{-1}) for Cr(VI) show that the adsorption of Cr(VI) on the composite surface is exothermic. The positive value of ΔH 152.0046 kJ mol^{-1} for Cr(III) recommends the exothermic nature for the adsorption of metal ions. The ΔS values are 0.0119 J K^{-1} mol^{-1} and 0.0024 J K^{-1} mol^{-1} for Cr(III) and Cr(VI) respectively. The positive values of ΔS for the adsorption of Cr(III) and Cr(VI) indicated the strong adsorption affinity of both states of the metal ions towards the composite and high degree of randomness at the adsorbent surface. The positive values of ΔG for Cr(VI) and Cr(III) at different temperatures showed the nonspontaneous adsorption nature which suggested the physisorption mode. The numerical values of the thermodynamic parameters (ΔS, ΔH and ΔG)[111] are summarized in Table 6 and the van't Hoff plot is given in Fig. 9(Z).

Table 6 vant's Haff parameters for the adsorption of chromium (VI and III) ions at silica-bound graphene oxide composite[a]

		Chromium(VI)			Chromium(III)		
T (K)	$1/T$ (K)	k (L mol^{-1})	ln K_L	$-\Delta G$ kJ mol^{-1}	K_L (L mol^{-1})	ln K_L	$-\Delta G$ kJ mol^{-1}
293	0.00341	25.5041	3.234	7.959	1.100	0.095	0.232
303	0.00330	25.563	3.373	8.497	1.305	0.672	2.264
313	0.00319	26.8202	3.278	8.553	2.545	0.9341	2.430
323	0.00309	18.065	2.851	7.656	13.02	2.53	6.794
333	0.00300	18.564	2.727	7.549	31.92	3.44	9.522

[a] The values of ΔH (kJ mol^{-1}) and ΔS (J K^{-1} mol^{-1}) are −12.193 and −0.01329 for Cr-VI while those of the Cr-III are 152–004 and 0.489 respectively.

Table 7 Removal of Cr-VI and Cr-III from real water samples collected from different sources

	Chromium-VI		Chromium-III	
Samples	Spiking amount (ppm)	% adsorption	Spiking amount (ppm)	% adsorption
Distilled water	100	99.862	100	99.654
Aitmaad steel mill	100	99.058	100	99.218
Deen leather industry	100	98.787	100	98.62

Application in real water samples. The newly synthesized composite was tried for the removal of chromium-VI and chromium-III from real water samples collected from different sources. The water samples were collected from a distillation plant, Aithimaad steel mill Chakdara Distt., Dir KP province of Pakistan, and site of the Deen leather industry Karachi Pakistan. The concentration of chromium(VI and III) metal ions was determined in all the samples after pre-treatment. All the samples were spiked by adding 100 mg L^{-1} of the metal ions followed by the addition of the composite (8 mg Cr(VI) and 6 mg Cr(III)). The optimized conditions were used for the adsorption of metal ions. The unabsorbed amounts of metal ions Cr(III) and Cr(VI) were determined by atomic absorption spectrometry. The adsorption of Cr(VI) was found to be 99.762%, 99.058%, and 98.887% in distilled water, wastewater of the steel industry, and wastewater of the leather industry respectively. Similarly, the adsorption of Cr(III) was found to be 99.654%, 99.218%, and 98.62% in distilled water, wastewater of the steel industry, and wastewater of the leather industry respectively. The values are given in Table 7. The variation in the percentage of adsorption of the metal ions in different samples collected from various industries may be due to the differences in pH and the presence of other pollutants which might suppress the adsorption of Cr(VI) and Cr(III).[112]

UV-visible spectrophotometric analysis of Cr(VI) and Cr(III) in real water samples. The real water samples were analysed for Cr(VI) and Cr(III) by ultra violet (UV)-visible spectrophotometry, as shown in Fig. 10. The absorbance peaks at 402 nm and 487 nm represent Cr(III) in the form of $CrCl_3$. The two narrow peaks at 270 nm and 380 nm are due to Cr(VI) present as $K_2Cr_2O_7$ in the solution. The difference in the peak of Cr(VI) from that of Cr(III) can be found in the literature.[113] The Cr(III) solution contains a supporting electrolyte (0.1 M HCl), which is responsible for the presence of Cr(III) as a mixture of $Cr(H_2O)_5OH_2^+$ and $Cr(H_2O)_6^{3+}$. The collected three samples of Cr(VI) and Cr(III) in distilled water, Deen leather industry, and Aithimaad steel mill gave different UV visible spectra after spiking with 100 mg L^{-1} of Cr(VI) and Cr(III) solutions. The relatively less difference in the UV-visible spectra of the samples collected from different areas is due to a slight difference in the pH values, temperature, and the presence of other contaminates, which resulted in relatively decreased absorbance.[114] A comparison of the adsorption capacity of the

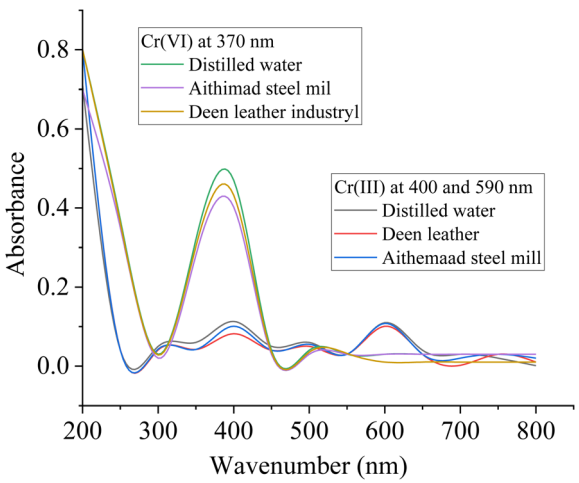

Fig. 10 UV-visible spectra for evaluating the removal efficiency of the composite towards Cr(VI) and Cr(III).

Table 8 Comparison of the adsorption capacity of the composite of current study with those of the reported adsorbents

Adsorbent	Adsorbate	Adsorption capacity ($mg\ g^{-1}$)	Ref.
Modified oak saw dust	Chromium(VI)	1.70	115
Cow hooves	Chromium(VI)	5.71	116
Neem sawdust	Chromium(VI)	58.82	117
Lakhra	Chromium(III)	2.61	118
Carbon nanotube	Chromium(VI)	85.83	119
Nitrogen doped	Chromium(VI)	227.27	120
Polymeric materials	Chromium(VI)	1185	121
Mixture by blast furnace slag (BFS)	Chromium(III)	43.16	122
N-Phenyl acrylamide modified Silica@GO	Chromium(VI)	298.507	Current study
	Chromium(III)	401.874	Current study

current adsorbent with those of the reported adsorbents is presented in Table 8.[115–122]

Conclusion

The sophisticatedly altered Fischer esterification protocol was applied for the synthesis of a silica monolith-anchored graphene oxide composite. The composite was modified with a polymer using *N*-phenyl acrylamide *via* RAFT polymerization. The composite synthesis was confirmed by FE-SEM, FTIR spectroscopy, XRD, zeta potential, EDX and BET/BJH analysis. The results of atomic absorption, UV-visible spectroscopy, and EDX confirmed the successful adsorption of Cr(VI) and Cr(III) at the composite surface. The synthesized polymer-bound composite exhibited many advantageous features such as the organic–inorganic hybrid nature, increased surface area, large pore size, monolithic architecture, mechanical strength, increased mass transfer kinetics for the adsorption process, high-throughput analysis, and the high regenerative ability after repeated uses for the adsorption of Cr(VI) and Cr(III). The adsorbent resulted in 99.762% adsorption of Cr(VI) and 99.654% adsorption of Cr(III) from the industrial effluents. The batch optimization studies helped in finding out the optimized values of different parameters pH $\sim$ 2, adsorbate con. $\sim$ 20 mg L^{-1}, contact time $\sim$ 80 min, adsorbent amount $\sim$ 8 mg for Cr(VI) and pH $\sim$ 5, adsorbate con. $\sim$ 20 mg L^{-1}, contact time $\sim$ 1 h, adsorbent amount $\sim$ 6 mg for Cr(III). The adsorption data best fitted to the pseudo 2nd-order kinetic model for Cr(VI) with R^2 of 0.996 and Cr(III) with R^2 of 0.999. Similarly, the data best fitted to the Langmuir adsorption isotherm having R^2 of 0.972 for Cr(VI), while Cr(III) follows the Freundlich adsorption isotherm model with R^2 of 0.983. The negative values of ΔH -12.193 kJ mol^{-1} $\sim$ Cr(VI) suggested the endothermic adsorption process, while the positive value (152.004 kJ mol^{-1}) $\sim$ Cr(III) suggested the exothermic adsorption nature of the process. The change in Gibbs free energy also goes in favour of the exothermic and spontaneous nature of the adsorption process, while the negative values of ΔS (-0.01329 kJ mol^{-1}) $\sim$ Cr(VI) suggest the higher affinity for Cr(VI) adsorption towards the adsorbent with no randomness, while the ΔS value of 0.00244 kJ mol^{-1} $\sim$ Cr(III) suggests a higher affinity of Cr(III) adsorption towards adsorbent with a higher degree of the randomness.

Conflicts of interest

There are no conflicts to declare.

Acknowledgements

This research was supported by the University of Malakand through Higher Education Commission (HEC) of Pakistan Project no: 20-14499/NRPU/R&D/HEC/2021 2021. The authors are grateful to the Researchers supporting Project No. (RSP-2023/R1), King Saud University, Riyadh, Saudi Arabia.

References

1 I. Osasona, K. Aiyedatiwa, K. Johnson, J. Faboya and O. L. Indonesian, *Journal Of Chemistry*, 2018, **18**(1), 145–152.
2 S. Chen, Q. Yue, B. Gao and X. Xu, *J. Colloid Interface Sci.*, 2010, **349**(1), 256–264.
3 P. K. Gautam, R. K. Gautam, S. Banerjee, M. C. Chattopadhyaya and J. D. Pandey, *J. Innovative Sci.*, 2016, **60**, 101–130.
4 V. H. T. Pham, J. Kim, S. Chang and W. Chung, *Microorganisms*, 2022, **10**(3), 610.
5 A. Kumar, D. Suman, B. Chiranjib and D. Siddhartha, *Chem. Eng. J.*, 2011, **173**, 135–143.
6 S. K. Kahlon, G. Sharma, J. M. Julka, A. S. Kumar, F. Sharma and F. J. Stadler, *J. Environ. Chem.*, 2018, **16**(3), 919–946.
7 C. Suhong, Y. Qinyan, G. Baoyu and X. Xing, *J. Colloid Interface Sci.*, 2010, **349**, 256–264.
8 C. A. Kozlowski and W. Walkowiak, *J. Water Resour.*, 2002, **36**, 4870–4876.
9 N. Kongsricharoern and C. Polprasert, *Water Sci. Technol.*, 1996, **34**, 109–116.
10 S. Rengaraj, K. H. Yeon and S. H. Moon, *J. Hazard. Mater.*, 2001, **87**, 273–287.
11 V. K. Gupta, A. K. Shrivastava and N. Jain, *J. Water Resour.*, 2001, **35**, 4079–4085.

12 D. Mohan, K. P. Singh and V. K. Singh, *J. Ind. Eng. Chem.*, 2005, **44**(4), 1027–1042.
13 A. Baran, E. Bıc and S. Hamarat-Baysal, *Bioresour. Technol.*, 2006, **98**, 661–665.
14 A. K. Tolkou, M. Mitrakas, I. A. Katsoyiannis, M. Ernst and A. I. Zouboulis, *Journal of Chemosphere*, 2019, **231**, 528–537.
15 H. Li, Y. Yin, L. Zhu, Y. Xiong, X. Li, T. Guo, W. Xing and Q. Xue, *J. Hazard. Mater.*, 2019, **373**, 725–732.
16 J. C. Kim, S. I. Oh, W. Kang, H. Y. Yoo, J. Lee and D. W. Kim, *J. Catal.*, 2019, **374**, 118–126.
17 W. Luo, F. I. Hai, W. E. Price, W. Guo, H. H. Ngo, K. Yamamoto and L. D. Nghiem, *Bioresour. Technol.*, 2014, **167**, 539–546.
18 J. Zhang, G. B. White, M. D. Ryan, A. J. Hunt and M. J. Katz, *ACS Sustain. Chem. Eng.*, 2014, **4**, 7186–7192.
19 M. A. Khan, *et al.*, *Groundw. Sustain. Dev.*, 2020, **11**, 100427.
20 Z. Shao, C. Huang, Q. Wu, Y. Zhao, W. Xu, Y. Liu, J. Dang and H. Hou, *J. Hazard. Mater.*, 2019, **378**, 120719.
21 D. Xu, F. Cheng, Q. Lu and P. Dai, *Ind. Eng. Chem. Res.*, 2014, **53**, 2625–2632.
22 Y. Wang, L. Yu, R. Wang, Y. Wang and X. Zhang, *J. Colloid Interface Sci.*, 2020, **574**, 74–86.
23 S. Bolisetty and R. Mezzenga, *Nat. Nanotechnol.*, 2016, **11**, 365–371.
24 H. Luan, J. Xu, Z. Tan, A. Zheng and H. Huang, *J. Chem. Technol. Biotechnol.*, 2019, **94**, 2816–2825.
25 Y. Yang, Z. Zheng, W. Ji, J. Xu and X. Zhang, *J. Hazard. Mater.*, 2020, 122686.
26 R. M. Richelle, K. Gangalakshmi, K. D. Mahaveer and K. Madhuprasad, *J. Hazard. Mater.*, 2021, **403**, 123605.
27 M. Ji and C. Kezheng, *Sep. Purif. Technol.*, 2020, **241**, 116705.
28 A. Einstein, B. Podolsky and N. Rosen, *Phys. Rev.*, 1935, **47**, 777–780.
29 X. Li, J. Liu, J. Feng, T. Wei, Z. Zhou, J. Ma, Y. Ren and Y. Shen, *J. Hazard. Mater.*, 2023, **445**, 130400.
30 L. Linqing, W. Jiahong and Z. Yanxin, *Microporous Mesoporous Mater.*, 2023, **347**, 112344.
31 R. M. Richelle, S. Ganesan, A. V. Kanalli, J. H. Young, K. D. Mahaveer and K. Madhuprasad, *J. Hazard. Mater.*, 2021, **416**, 125941.
32 P. Loris, F. Iolanda, P. Antonella, S. Maria, S. Ilaria and V. Marco, *Appl. Sci.*, 2020, **10**, 1925.
33 I. Duru, D. Ege and A. R. Kamali, *J. Mater. Sci.*, 2016, **51**, 6097–6116.
34 A. Ali, M. Aamir, K. H. Thebo and J. Akhtar, *Chem. Rec.*, 2020, **20**(4), 344–354.
35 R. Sitko, M. Musielak, M. Serda, E. Talik, B. Zawisza, A. Gagor and M. Malecka, *Sep. Purif. Technol.*, 2021, **254**, 11760.
36 J. Shi, J. Sun, T. Wang, L. Zeng and G. Jiang, *Chem. Eng.*, 2011, **50**, 5913–5917.
37 A. I. A. Sherlala, A. A. A. Raman, M. M. Bello and A. Asghar, *Chemosphere*, 2018, **193**, 1004–1017.
38 X. Zhao, X. Xu, J. Teng, N. Zhou, Z. Zhou, X. Jiang, F. Jiao and J. Yu, *Ecotoxicology and Environmental Safety*, 2019, **176**, 11–19.
39 S. Yang, D. Zhang, H. Cheng, Y. Wang and J. Liu, *Anal. Chim. Acta*, 2009, **1074**, 54–61.
40 H. Barrak, R. Ahmedi, P. Chevallier, A. M'Nif, G. Laroche and A. H. Hamzaoui, *Sep. Purif. Technol.*, 2019, **222**, 145–151.
41 S. Dey, S. Podder, A. Roychowdhury, D. Das and C. Ghosh, *J. Environ. Manage.*, 2018, **211**, 356–366.
42 M. Li, S. Tang, Z. Zhao, X. Meng, F. Gao, S. Jiang and C. Feng, *Chem. Eng. J.*, 2020, **386**, 123947.
43 Z. Meixing, Y. Jiahui, G. Xinxiang, Y. Li, L. Zhenxing, C. Shihai and Y. Jing, *J. Chromatogr. A*, 2019, **1598**, 20–29.
44 M. Khan, M. Muhammad, Z. A. AlOthman, w. J. Cheong and F. Ali, *Sci. Rep.*, 2022, **12**, 21027.
45 K. Xiang-Ping, Z. Bao-Hua and W. Juan, *J. Agric. Food Chem.*, 2021, **69**, 6735–6754.
46 M. Ma, H. Li, Y. Xiong and F. Dong, A review, *Mater. Des.*, 2021, **198**, 109367.
47 A. A. Iqbal, N. Sakib, A. P. Iqbal and D. M. Nuruzzaman, *Materialia*, 2020, **12**, 100815.
48 M. Hayati-Ashtiani, *et al.*, *Part. Part. Syst. Charact.*, 2011, **28**, 71–76.
49 C. Paluszkiewicz, M. Holtzer and A. Bobrowski, *J. Mol. Struct.*, 2008, **880**, 109–114.
50 J. D. Clogston and A. K. Patri, *Methods in Molecular Biology*, 2011, p. 697.
51 F. Ali and W. J. Cheong, *J. Sep. Sci.*, 2014, **37**, 3426–3434.
52 N. I. Zaaba, K. L. Foo, U. Hashim, S. J. Tan, W. W. Liu and C. H. Voon, *Procedia Eng.*, 2017, **184**, 469–477.
53 J. Chen, Y. Li, L. Huang, C. Li and G. Shi, *Carbon*, 2015, **81**, 826–834.
54 R. Kumar, M. Kumar, A. Kumar, R. Singh, R. Kashyap, S. Rani and D. Kumar, *Materials Today*, 2019, **18**, 1556–1561.
55 S. Agarwal, N. Sadeghi, I. Tyagi, V. K. Gupta and A. Fakhri, *J. Colloid Interface Sci.*, 2016, **478**, 430–438.
56 A. Ali, F. Ali and W. J. Cheong, *J. Chromatogr. A*, 2017, **1525**, 79–86.
57 M. Beija, J. D. Marty and M. Destarac, *Polym. Sci.*, 2011, **36**(7), 845–886.
58 G. Moad, M. Chen, M. Häussler, A. Postma, E. Rizzardo and S. H. Thang, *Polym. Chem.*, 2011, **2**(3), 492–519.
59 A. Favier and M. T. Charreyre, *Macromol. Rapid Commun.*, 2006, **27**(9), 653–692.
60 S. Perrier and P. Takolpuckdee, *J. Polym. Sci., Part A: Polym. Chem.*, 2005, **43**(22), 5347–5393.
61 J. Jiao, P. Liu, L. Wang and Y. Cai, *J. Polym. Res.*, 2013, **20**(8), 1–8.
62 M. P. Desimone, G. Grundmeier, G. Gordillo and S. N. Simison, *Electrochim. Acta*, 2011, **56**(8), 2990–2998.
63 P. Ragavendran, D. Sophia, C. Arul Raj and V. K. Gopalakrishnan, *Pharmacologyonline*, 2011, **1**, 358–364.
64 S. B. Daffalla, H. Mukhtar and M. S. Shaharun, *PloS One*, 2020, **15**(12), 0243540.
65 V. Hospodarova, E. Singovszka and N. Stevulova, *Am. J. Anal. Chem.*, 2018, **9**(6), 303–310.

66 J. Zhang, Y. Duan, H. Sato, H. Tsuji, I. Noda, S. Yan and Y. Ozaki, *Macromolecules*, 2005, **38**(19), 8012–8021.
67 J. J. Moyano, J. Loizillon, D. Pérez-Coll, M. Belmonte, P. Miranzo, D. Grosso and M. I. Osendi, *J. Eur. Ceram. Soc.*, 2021, **41**(4), 2908–2917.
68 B. Ramezanzadeh, Z. Haeri and M. Ramezanzadeh, *Chem. Eng. J.*, 2016, **303**, 511–528.
69 K. I. Panayotov, D. A. Mihaylov, M. Y. Ivanova, E. Z. Chakarova, K. K. Andonova and N. L. Drenchev, *Chem. Rev.*, 2020, **121**, 1286–1424.
70 W. C. Li, A. H. Lu and F. Schüth, *Chem. Mater.*, 2005, **17**(14), 3620–3626.
71 R. M. N. M. Rathnayake, H. W. M. A. C. Wijayasinghe, H. M. T. G. A. Pitawala, M. Yoshimura and H. H. Huang, *Appl. Surf. Sci.*, 2017, **393**, 309–315.
72 K. X. Sheng, Y. X. Xu, L. I. Chun and G. Q. Shi, *New Carbon Mater.*, 2011, **26**(1), 9–15.
73 S. Agarwal, N. Sadeghi, I. Tyagi, V. K. Gupta and A. Fakhri, *J. Colloid Interface Sci.*, 2016, **478**, 430–438.
74 K. Krishnamoorthy, M. Veerapandian, R. Mohan and S. J. Kim, *Appl. Phys. A: Mater. Sci. Process.*, 2011, **106**(3), 501–506.
75 K. I. Hadjiivanov, D. A. Panayotov, M. Y. Mihaylov, E. Z. Ivanova, K. K. Chakarova, S. M. Andonova and N. L. Drenchev, *Chem. Rev.*, 2020, **121**, 1286–1424.
76 J. Q. Dalagan and E. P. Enriquez, *Mater. Sci. Appl.*, 2014, **37**, 589–595.
77 V. Agarwal and P. B. Zetterlund, *Chem. Eng. J.*, 2021, **405**, 127018.
78 P. K. Deshmukh, S. H. Lakade, U. R. Jaiswal, M. T. Harde and M. P. More, *Mater. Technol.*, 2021, 1–14.
79 I. Izquierdo-Barba, M. Vallet-Regí, N. Kupferschmidt, O. Terasaki, A. Schmidtchen and M. Malmsten, *Biomaterials*, 2009, **30**, 5729–5736.
80 X. Wang, Z. Li, Q. Ma, J. Li and M. Zhu, *Chem. Eng. J.*, 2015, **273**, 630–637.
81 E. Asadi, S. A. Deilami, M. Abdouss, D. Kordestani, A. Rahimi and S. Asadi, *Korean J. Chem. Eng.*, 2014, **31**, 1028–1035.
82 R. Song, X. Hu, P. Guan, J. Li, L. Qian, C. Wang and Q. Wang, *Appl. Surf. Sci.*, 2015, **332**, 159–166.
83 B. Ren, Q. Zhang, X. Zhang, L. Zhao and H. Li, *RSC Adv.*, 2018, **8**, 38157–38165.
84 H. Essebaai, H. Lgaz, A. A. Alrashdi, A. Habsaoui, A. Lebkiri, S. Marzak and E. H. Rifi, *Int. J. Environ. Sci. Technol.*, 2022, **19**, 2443–2454.
85 K. Krishnamoorthy, M. Veerapandian, K. Yun and S. J. Kim, *Carbon*, 2013, **53**, 38–49.
86 H. Tang, Y. Zhao, S. Shan, X. Yang, D. Liu, F. Cui and B. Xing, *Environ. Sci.*, 2018, **5**, 2357–2367.
87 Y. Chen, S. An, J. Sun, J. Gao and L. Qian, *Materials*, 2018, **11**(269), 2–12.
88 D. Mohan, K. P. Singh and V. K. Singh, *J. Hazard. Mater.*, 2006, **135**(1–3), 280–295.
89 A. A. Moosa, A. M. Ridha and I. N. Abdullah, *Int. J. Innov. Res. Technol.*, 2015, **4**(2), 275–282.
90 E. Asadi, S. A. Deilami, M. Abdouss, D. Kordestani, A. Rahimi and S. Asadi, *Korean J. Chem. Eng.*, 2014, **31**, 1028–1035.
91 Y. Yang, X. Ma, C. Yang, Y. Wang, J. hao and Q. Zhang, *Chem. Eng. J.*, 2021, **430**, 132999.
92 Y. An, H. Zheng, Z. Yu, Y. Sun, Y. Wang, C. Zhao and W. Ding, *J. Hazard. Mater.*, 2020, **381**, 120971.
93 Q. U. Ain, U. Rasheed, M. Yaseen, H. Zhang, R. He and Z. Tong, *Appl. Surf. Sci.*, 2020, **514**, 145929.
94 S. Debnath, A. Maity and K. Pillay, *J. Environ. Chem. Eng.*, 2014, **2**(2), 963–973.
95 H. Lin, S. Han, Y. Dong and Y. He, *Appl. Surf. Sci.*, 2017, **412**, 152–159.
96 R. M. Ali, H. A. Hamad, M. M. Hussein and G. F. Malash, *Ecol. Eng.*, 2016, **91**, 317–332.
97 L. Zhang, W. Xia, X. Liu and W. Zhang, *J. Mater. Chem. A*, 2015, **3**(1), 331–340.
98 D. Božić, V. Stanković, M. Gorgievski, G. Bogdanović and R. Kovačević, *J. Hazard. Mater.*, 2009, **171**(1–3), 684–692.
99 P. A. G. Cormack and A. Z. Elorza, *J. Chromatogr. A*, 2004, **804**, 173–182.
100 R. Saadi, Z. Saadi, R. Fazaeli and N. E. Fard, *Korean J. Chem. Eng.*, 2015, **32**, 787–799.
101 P. Ammendola, F. Raganati and R. Chirone, *Chem. Eng. J.*, 2017, **322**, 302–313.
102 M. K. Zahra and M. Nahid, *Inorg. Nano-Met. Chem.*, 2019, **49**, 231–239.
103 R. J. Umpleby, S. C. Baxter, M. Bode, J. K. Berch, R. N. Shah and K. D. Shimizu, *Anal. Chim. Acta*, 2001, **435**, 35–42.
104 S. Banerjee and M. C. Chattopadhyaya, *Arabian J. Chem.*, 2017, **10**, S1629–S1638.
105 C. Wu, S. Zhang, G. Nie, Z. Zhang and J. Wang, *J. Environ. Sci.*, 2011, **23**, 1524–1532.
106 P. S. Kumar and K. Kirthika, *J. Eng. Sci. Technol.*, 2009, **4**, 351–363.
107 W. Astuti, M. A. Mahardhika, D. A. Putri, M. Rohman, M. F. Sihab, T. Sulistyaningsih and E. F. Irchamsyah, *Mater. Sci. Eng.*, 2019, **625**, 012025.
108 D. Grekov, P. Pré and B. J. Alappat, *Renewable Sustainable Energy Rev.*, 2020, **124**, 109743.
109 S. Karaca, A. Gürses, M. Ejder and M. Açıkyıldız, *J. Colloid Interface Sci.*, 2004, **277**, 257–263.
110 Y. Liu, *et al.*, *J. Chem. Eng. Data*, 2009, **54**(7), 1981–1985.
111 L. Xia, E. Akiyama, G. Frankel and R. McCreery, *J. Electrochem. Soc.*, 2000, **147**, 2556–2562.
112 C. K. B. Lauren and M. Bruce, *Crystals*, 2021, **11**, 443.
113 M. A. Salam, S. A. Kosa and A. A. Al-Beladi, *J. Mol. Liq.*, 2017, **241**, 469–477.
114 M. E. Argun, S. Dursun, C. Ozdemir and M. Karatas, *J. Hazard. Mater.*, 2007, **141**, 77–85.
115 J. Qu, W. Zhang, F. Bi, S. Yan, X. Miao, B. Zhang and Y. Zhang, *Environ. Pollut.*, 2022, **306**, 119398.
116 V. Vinodhini and N. Das, *J. Sci. Res.*, 2009, **4**(4), 324–329.
117 A. Jamil, U. Shafiquea, M. Salmana, U. Z. Waheed, A. Shafique and M. A. Jesús, *J. Hazard. Mater.*, 2009, **171**, 797–801.

118 N. F. Fahim, B. N. Barsoum, A. E. Eid and M. S. Khalil, *J. Hazard. Mater.*, 2006, **136**(2), 303–309.
119 A. S. K. Kumar, S. J. Jiang and W. L. Tseng, *J. Mater. Chem. A*, 2015, **3**(13), 7044–7057.
120 J. Chen, Y. Li, L. Wang, Z. Zhang, D. Lu, M. Lu and M. Chopp, *Stroke*, 2001, **32**(4), 1005–1011.
121 X. Yuan, J. Li, L. Luo, Z. Zhong and X. Xie, *Polymers*, 2023, **15**(2), 388.
122 C. Toufik, K. Ouahida, C. Sana and B. Aatmane, *Anal. Bioanal. Chem. Res.*, 2023, **10**(3), 251–268.